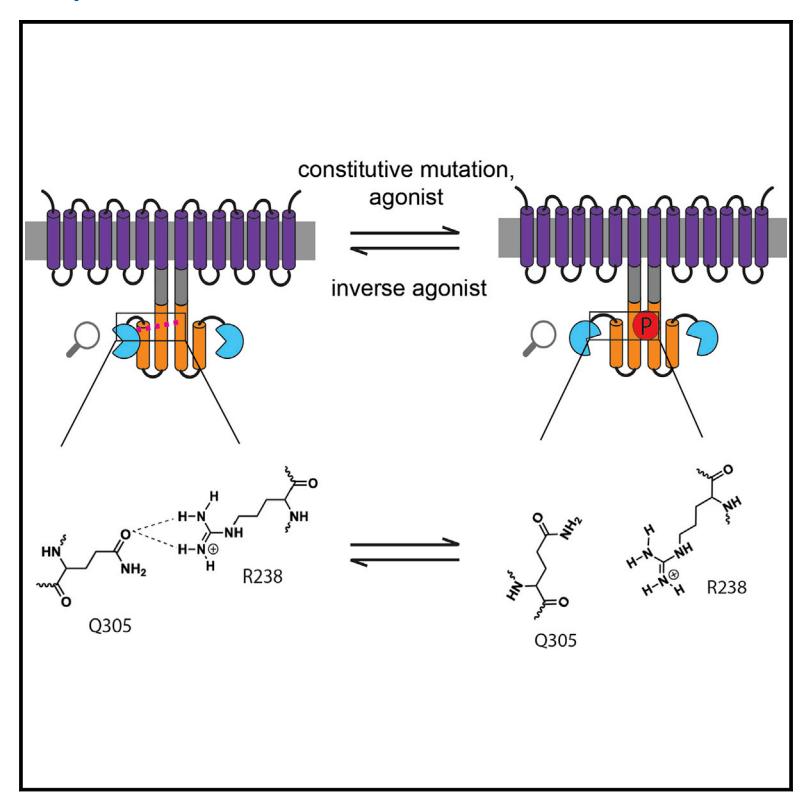
## **Cell Chemical Biology**

# Identification of a Molecular Latch that Regulates Staphylococcal Virulence

#### **Graphical Abstract**



#### **Authors**

Qian Xie, Aishan Zhao, Philip D. Jeffrey, ..., Howard A. Stone, Richard P. Novick, Tom W. Muir

#### Correspondence

muir@princeton.edu

#### In Brief

In this work, Xie et al. report the structure of a chimeric protein containing the complete HK module of AgrC, the histidine kinase involved in *S. aureus* agr quorum sensing. Structure-guided biochemical analysis reveals that activation of AgrC involves disruption of an intrasteric inhibitory docking interaction in the AgrC dimer.

#### **Highlights**

- Structure of the full HK module of the S. aureus histidine kinase AgrC
- The DHp-CA docking interaction precludes AgrC autophosphorylation
- R238-Q305 hydrogen bond is key to sequestering AgrC in its inactive state
- The conformation of the S helix and the stability of the DHp-CA interface are coupled

#### **Data Resources**

6E52 6E95





# Identification of a Molecular Latch that Regulates Staphylococcal Virulence

Qian Xie,<sup>1</sup> Aishan Zhao,<sup>1</sup> Philip D. Jeffrey,<sup>2</sup> Minyoung Kevin Kim,<sup>1,6</sup> Bonnie L. Bassler,<sup>2,4</sup> Howard A. Stone,<sup>3</sup> Richard P. Novick,<sup>5</sup> and Tom W. Muir<sup>1,7,\*</sup>

https://doi.org/10.1016/j.chembiol.2019.01.006

#### **SUMMARY**

Virulence induction in the Staphylococcus aureus is under the control of a quorum sensing (QS) circuit encoded by the accessory gene regulator (agr) locus. Allelic variation within agr produces four QS specificity groups, each producing a unique secreted autoinducer peptide (AIP) and receptor histidine kinase (RHK), AgrC. Cognate AIP-AgrC interactions activate virulence through a two-component signaling cascade, whereas non-cognate pairs are generally inhibitory. Here we pinpoint a key hydrogen-bonding interaction within AgrC that acts as a switch to convert helical motions propagating from the receptor sensor domain into changes in inter-domain association within the kinase module. AgrC mutants lacking this interaction are constitutively active in vitro and in vivo, the latter leading to a pronounced attenuation of S. aureus biofilm formation. Thus, our work sheds light on the regulation of this biomedically important RHK.

#### INTRODUCTION

Two-component signaling (TCS) is prevalent in bacteria and is essential for their adaptation to a changing environment (Capra and Laub, 2012). Among Gram-positive bacteria, arguably the best-characterized TCS system lies within the *agr* quorum sensing (QS) circuit in *Staphylococci*. Activation of *agr* QS is critical to the regulation of virulence within this genus, which includes the commensal pathogen *Staphylococcus aureus* (Thoendel et al., 2011). Consequently, there is a pressing need to understand the molecular mechanisms attendant to every stage in this signaling process (Wang and Muir, 2016).

The *agr* locus contains an operon encoding four proteins, AgrA-D, that together constitute the core QS circuit. The activity of the integral membrane protease AgrB is required for processing of AgrD into the secreted signaling pheromone, namely the

autoinducer peptide (AIP) (Zhang et al., 2002). Upon reaching a threshold concentration, the AIP binds to the transmembrane receptor histidine kinase (RHK), AgrC, leading to its autophosphorylation on a histidine residue (George Cisar et al., 2009). The phosphoryl group is subsequently transferred to the response regulator AgrA, enhancing its DNA binding capability through dimerization (Srivastava et al., 2014; Sidote et al., 2008). Phosphorylated AgrA drives the transcription of the agr QS genes, thereby creating a positive feedback loop, and an effector RNA molecule, RNAIII, which regulates the expression of multiple virulence genes (Novick et al., 1993, 1995).

A remarkable feature of agr is the allelic variation found within the operon encoding the QS circuit (Dufour et al., 2002). Within S. aureus this leads to four specificity groups, each producing a unique AIP/AgrC pair. Cognate AIP-AgrC interactions activate virulence, whereas non-cognate pairs are generally inhibitory (Ji et al., 1997). This phenomenon represents a natural form of bacterial interference, and has clear ramifications for the development of therapeutic strategies (Gordon et al., 2013). Indeed, extensive medicinal chemistry efforts have afforded a number of peptidic compounds that function as global inhibitors of the agr response, i.e., they antagonize AgrC from all four S. aureus groups (Lyon et al., 2000; Tal-Gan et al., 2013; Vasquez et al., 2017). While attenuation of S. aureus virulence by blocking the agr response has obvious appeal, and is effective in animal models of infection (Mayville et al., 1999; Wright et al., 2005), the opposite approach, activation of the agr response, has also been proposed as a therapeutic strategy (Wang and Muir, 2016). This idea is based on the link between the agr response and the stability of S. aureus biofilms (Boles and Horswill, 2008; Kong et al., 2006). Activation of agr leads to biofilm disruption, which could have benefit in enhancing the susceptibility to antibiotic treatment, thus preventing persistent infections (Vuong et al., 2000; Kim et al., 2017).

Exploiting *agr* for the development of novel therapies will rely on a full understanding of the mechanisms underlying agonism and antagonism of the TCS. This is complicated by the nature of AgrC, a 430-residue integral membrane protein that forms an obligate dimer (George Cisar et al., 2009). The receptor contains two functional modules (Figure 1A), a membrane embedded sensor that binds AIP and a cytoplasmic histidine



<sup>&</sup>lt;sup>1</sup>Department of Chemistry, Princeton University, Frick Chemistry Laboratory, Washington Road, Princeton, NJ 08544-0015, USA

<sup>&</sup>lt;sup>2</sup>Department of Molecular Biology, Princeton University, Schultz Laboratory, Washington Road, Princeton, NJ 08544, USA

<sup>&</sup>lt;sup>3</sup>Department of Mechanical and Aerospace Engineering, Princeton University, Engineering Quadrangle, Olden Street, Princeton, NJ 08544, USA

<sup>&</sup>lt;sup>4</sup>Howard Hughes Medical Institute, Chevy Chase, MD 20815, USA

<sup>&</sup>lt;sup>5</sup>Skirball Institute, Department of Microbiology, NYU Medical Center, 540-562 First Avenue, New York, NY 10016, USA

<sup>&</sup>lt;sup>6</sup>Present address: Department of Medicine, Yonsei University College of Medicine, Seoul 03725, South Korea

<sup>&</sup>lt;sup>7</sup>Lead Contact

<sup>\*</sup>Correspondence: muir@princeton.edu

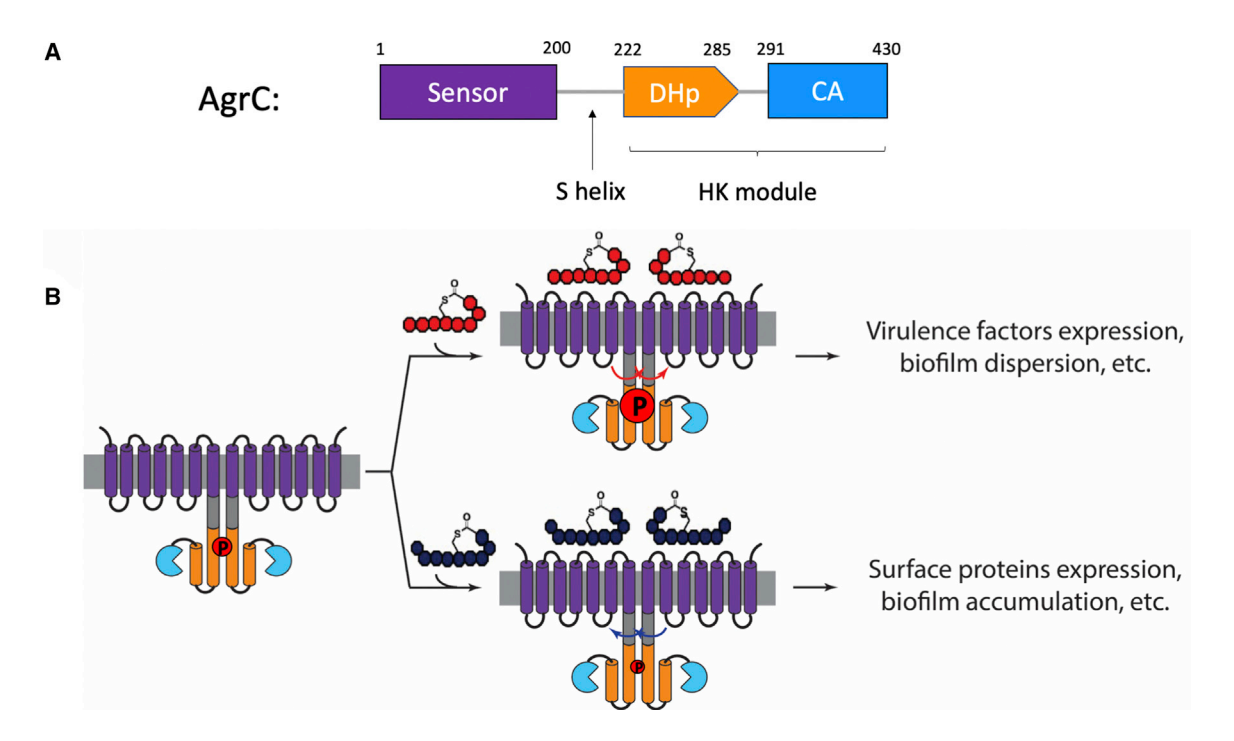


Figure 1. Overview of the AgrC Structure and Regulation

(A) Domain organization of AgrC.

(B) Schematic of the proposed model for AgrC regulation (Wang et al., 2014a). Agonist (in red) or inverse agonist (in blue) binding to AgrC sensor domain elicits opposite rotation in the signaling helix (S helix), which results in differential AgrC autokinase activity and alters downstream output.

kinase (HK). Unlike prototypical HKs, no auxiliary domains (e.g., HAMP or PAS domains) exist between the two functional modules in AgrC. Instead, they are linked via a short peptide sequence with high helical propensity (Wang et al., 2014a), which we term the signaling helix or S helix (Figure 1A). The cytoplasmic HK module of AgrC is composed of a dimerization and histidine phosphotransfer (DHp) domain that harbors the phosphoacceptor histidine (His239), and a catalytic and ATP binding (CA) domain. The HK functions both as an autokinase and as a phosphotransferase; however, it lacks any phosphatase activity and hence supports unidirectional signal propagation (Wang et al., 2014a).

Reconstitution of full-length AgrC from different specificity groups (AgrC-I, -II, and -III) into nanometer-scale lipid bilayer discs (nanodiscs) has led to important insights into the functioning of the TCS system (Wang et al., 2014a, 2017). In the apo form, AgrC has basal autokinase activity, which is stimulated by binding of the cognate AIP. Interestingly, depending on the group of origin, non-cognate AIPs can act as neutral antagonists (competitive ligands that do not alter the basal autokinase activity, e.g., AIP-III on AgrC-I) or inverse agonists (ligands that lower basal autokinase activity, e.g., AIP-II on AgrC-I) of the receptor. Moreover, certain synthetic AIP analogs can act as partial agonists of AgrC (Johnson et al., 2015; Lyon et al., 2002). Thus, the HK activity of the receptor appears to be tunable depending on the ligand state. Notably, this exact behavior can be recapitulated by imposing rotational torque on the S helix using chimeric constructs in which the sensor domain is replaced by the GCN4 leucine zipper (Wang et al., 2014a). These experiments imply that HK regulation is somehow linked to helical twisting motions propagating through the S helix into the DHp (Figure 1B). Analogous activation models involving rotary movements within DHp domains, induced by input signals, have been proposed for several other sensor HKs (Berntsson et al., 2017; Albanesi et al., 2009; Casino et al., 2009).

Despite the significant progress made on elucidating the agr signaling mechanism, major gaps in our knowledge remain. It is unclear how ligand engagement with the sensor domain of AgrC influences the conformation of the S helix. Equally unclear is how conformational changes in this region translate to altered HK activity. Structural studies on several HK modules have revealed interactions between the CA and DHp domains that are incompatible with histidine autophosphorylation (Marina et al., 2005; Mechaly et al., 2014; Casino et al., 2009). This has led to allosteric activation models in which the CA domain becomes unleashed from a sequestered state, resulting in increased HK activity. While the structure of the isolated CA domain of AgrC has been determined (Srivastava et al., 2014), it has remained unclear how, or if, this domain interacts with the remainder of the HK module as a function of AIP binding to the sensor domain. Here we report a crystal structure of the AgrC HK module trapped in the apo form. We find that the CA domain docks against the DHp helices in a manner that prevents histidine autophosphorylation. Structure-guided mutagenesis reveals a key hydrogen-bonding interaction at the interface essential to this sequestration. Collectively, our studies identify the nexus between mechanical motions originating from AIP ligand binding to the AgrC sensor, propagated through the S helix, and changes in inter-domain association and enzymatic output within the HK module.

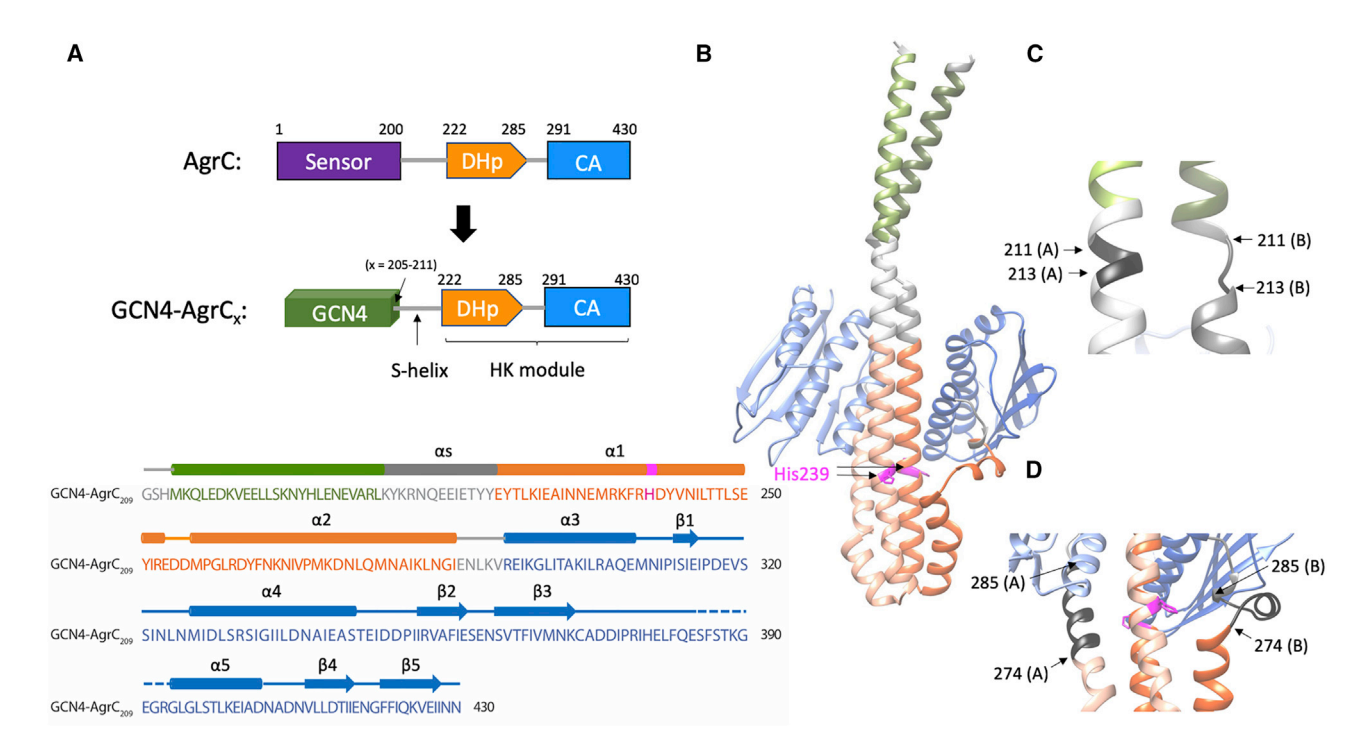


Figure 2. X-Ray Crystal Structure of the GCN4-AgrC Chimera

(A) Design of the GCN4-AgrC chimeric constructs used in the crystallization screen. The GCN4 coiled coil is used to replace AgrC-I sensor domain and is fused to AgrC at different positions (205–211) in the S helix. These constructs are denoted as GCN4-AgrC<sub>x</sub>, where x represents the amino acid number of AgrC-I at the fusion junction (top). The primary sequence of the GCN4-AgrC<sub>209</sub> chimera is shown with the secondary structure elements indicated on top (bottom). (B) Crystal structure of the GCN4-AgrC<sub>209</sub> dimer (PDB: 6E52). The GCN4 coiled coil is colored olive, the DHp domain coral, the CA domain blue, and the interdomain linker gray. Chain A is in light color and chain B is in dark color. The phosphoacceptor His239 are highlighted in magenta. (C and D) Asymmetry within the GCN4-AgrC<sub>209</sub> dimer resulting from helical unwinding at two locations in chain B: residues 211–213 at the junction between GCN4 and the DHp domain (C) and residues 274–285 within the  $\alpha$ 2 helix (D). The two segments are highlighted in black in both chains for comparison.

#### **RESULTS**

Understanding of AgrC signaling requires structural information on the RHK in different activity states. Ideally, such analyses would involve full-length AgrC dimers bound to different AIP agonists and antagonists. This is made extremely challenging by the polytopic nature of the transmembrane sensor module and the absolute requirement for a lipid bilayer for signal transduction (Wang et al., 2014a). Given these issues, we imagined that a more expeditious path to investigate how the S helix conformation regulates AgrC autokinase activity might involve exploiting the aforementioned GCN4 fusion strategy. This system obviates the need for the sensor module, affording well-behaved soluble protein, yet still allows the activity state of the kinase to be tuned by adjusting the fusion junction between the leucine zipper and the S helix (Figure 2A). Importantly, GCN4-AgrC HK fusion chimeras phenocopy full-length AgrC in different ligand bound forms (i.e., the "AIP-II bound," versus the "apo," versus the "AIP-I bound") (Wang et al., 2014a). Thus, we reasoned that structural information obtained on a GCN4-HK fusion would be directly relevant to the regulation of the HK module in the context of full-length AgrC in the corresponding activity state.

#### **Structure Determination**

We successfully obtained diffraction quality crystals for a GCN4-HK construct in which the leucine zipper is linked to AgrC-I at

residue 209, designated as GCN4-AgrC<sub>209</sub> henceforth (Figure 2A). GCN4-AgrC<sub>209</sub> has basal autokinase activity and is predicted to mimic AgrC-I conformation in its apo form (Wang et al., 2014a). Despite extensive screening efforts, we were unable to crystallize chimeras corresponding to the active state of the receptor. We speculate that enhanced mobility of the CA domain within such constructs disfavors crystal packing (see below). The structure of GCN4-AgrC<sub>209</sub> was determined by combination of molecular replacement, using the AgrC CA domain structure (PDB: 4BXI) as the search model, and SAD phasing using a selenomethionine substituted version of the protein. The final structure was refined against a 2.25-Å dataset (Table S1). It is worth noting that we were also able to crystallize GCN4-AgrC209 in the presence of 2 mM Mg<sup>2+</sup>-AMPPCP, but no electron density indicative of the co-factor was observed (data not shown). This observation is consistent with the low-affinity AgrC has for ATP  $(Km_{ATP} = \sim 2 \text{ mM})$  (Wang et al., 2014a).

#### Overall Structure of GCN4-AgrC<sub>209</sub>

The asymmetric unit of the GCN4-AgrC<sub>209</sub> crystal contains one protein dimer (Figure 2B). Within this dimer, the GCN4 sequence (residues 4–28) adopts the canonical leucine zipper structure (as confirmed by SOCKET [Walshaw and Woolfson, 2001]) with a helical crossing angle of 15.9°. The C-terminal CA domain (AgrC-I residues 291–430) adopts the characteristic  $\alpha/\beta$  sandwich fold of the GHKL ATPase superfamily (Dutta and Inouye,

2000). The structure of each CA domain within the dimer is similar to that of the isolated domain (PDB: 4BXI; main-chain root-mean-square deviation = 2.36 Å in protomer A and 0.98 Å in protomer B, excluding the ATP lid residues 382-397). Residues that form part of the ATP lid are not resolved in our model (residues 385-390 in chain A and residues 375-395 in chain B), likely due to flexibility in this region (Figure S1A). The central DHp domain (AgrC-I residues 222-285) consists of an antiparallel  $\alpha$ -helical hairpin that dimerizes via a hydrophobic core. The phosphoacceptor His239 is located in the middle of the first  $\alpha$  helix (DHp  $\alpha$ 1) and is solvent exposed in both protomers (Figures 2A and S1B). Above the plane of His239, the two DHp  $\alpha$ 1 helices are nearly parallel, with a helical crossing angle of 11.8°. Unlike most HKs (Mechaly et al., 2014; Ferris et al., 2012; Casino et al., 2014), AgrC lacks a proline residue at the fifth residue C-terminal to the histidine (part of the H-box motif). Likely as a consequence, the bend in the DHp  $\alpha 1$  helix below the plane of His239 is less pronounced than observed in other HK structures (Figure S1C). The  $\alpha$ 2 helices from each protomer are splayed apart at their C termini, with the result that the four-helix bundle is only maintained for about two helical turns at the base of the DHp (Figure 2B). GCN4 and the DHp domain are linked by a stretch of the S helix (AgrC-I residues 209-221), while a short five-amino acid residue loop (AgrC-I residues 286-290) connects the DHp and CA domains (Figures 2A and 2B).

Unlike many HK structures assigned to the inactive state (Marina et al., 2005; Casino et al., 2009; Albanesi et al., 2009), the domain arrangement in the GCN4-AgrC<sub>209</sub> dimer is asymmetric (Figure 2B). The symmetry breaks mainly at two points. The first is located close to the fusion junction between GCN4 and AgrC (Figure 2C). While GCN4 and the S helix form a continuous helix in chain A, in chain B the helix unwinds into a random coil between residues Lys211 and Asn213. This disruption is needed to accommodate the inter-chain helical packing arrangements within both GCN4 and the DHp domain. A similar helical unwinding was observed close to the fusion junction in the chimeric structure of the Af1503 HAMP domain fused to the EnvZ HK module (Ferris et al., 2014). The second symmetry break is located in the C-terminal half of the DHp α2 helix (Figure 2D). While residues Asn274-Ile285 assume an  $\alpha$ -helical structure in chain A, in chain B they are largely deformed. This asymmetry appears to be influenced by crystal packing interactions involving an adjacent inverted dimer in the lattice (Figure S1D). We note, however, that models for HK activation have been proposed that involve partial cracking of the DHp α2 helix (Dago et al., 2012). Indeed, an asymmetric distortion in this region is observed in the crystal structure of the blue-lightregulated sensor HK, YF1 (Diensthuber et al., 2013). Thus, the helix deformation observed here might reflect the intrinsic structural plasticity of this region and, as such, represent a required step toward attaining the active conformation.

### The GCN4-AgrC Chimeric Construct Autophosphorylates in *trans*

Previous studies have suggested the handedness of the loop connecting the two DHp  $\alpha$  helices serves as a predictor of whether HK autophosphorylation occurs in cis (i.e., within a protomer) or in trans (Ashenberg et al., 2013). According to this model, when viewed down the central axis of the DHp four-helix

bundle, kinases with a left-handed loop (e.g., HK853 and PhoR) carry out *cis* autophosphorylation, while those with a right-handed loop (e.g., EnvZ and CpxA) autophosphorylate in *trans* (Figure 3A). By this measure, GCN4-AgrC<sub>209</sub> is predicted to undergo autophosphorylation in *cis*. Previous cell-based studies indicate, however, that full-length AgrC undergoes autophosphorylation in *trans* (George Cisar et al., 2009). We imagined two possibilities to account for this apparent discrepancy: either the GCN4 fusion somehow perturbs the autophosphorylation mode of the HK, or alternatively, AgrC is an exception to this rule. Note that the latter possibility is not without precedent (Ashenberg et al., 2013).

To explore cis versus trans autophosphorylation, we designed an experiment based on functional complementation of HK mutants that either lack the phosphoacceptor histidine (H239Q) and/or that abolish ATP binding (G394A/G396A). As a template for these studies, we employed a GCN4-AgrC-I chimera (GCN4-AgrC<sub>207</sub>) with robust kinase activity. Two tagged versions of this construct were employed, one fused with an N-terminal His 6-MBP tag and one with a C-terminal Strep-tag (Figure 3B; Table S2). This allowed heterodimers to be isolated by tandem purification and discriminated based on size using native PAGE. Since our workflow necessitated a reconstitution step to form the heterodimers, we initially confirmed that the wildtype GCN4-AgrC<sub>207</sub> (Figure 3B, construct 1) retains full autokinase activity following a refolding protocol (Figure 3C, lanes 1 and 2). Additional controls confirmed that GCN4-AgrC207 constructs harboring the H239Q mutation, the G394A/G396A mutation or a combination thereof were inactive (Figure 3B, constructs 2, 3, and 5; Figure 3C, lanes 3, 4, and 7, respectively). Critically, a strong phospho-histidine (pHis) signal was associated with the heterodimer reconstituted from constructs 2 and 3 (Figure 3C, lane 5), a result that can only be explained through autophosphorylation in trans. The lower pHis band in lane 5, which has the same size as construct 3, results from spontaneous subunit exchange of the phosphorylated heterodimer back to constituent homodimers, since no autophosphorylation was observed when construct 3 was treated with ATP (Figure 3C, lane 4). The question of whether cis autophosphorylation can also occur was addressed by forming a heterodimer from the His<sub>6</sub>-MBP-tagged wild-type GCN4-AgrC<sub>207</sub> (Figure 3B, construct 4) and the Strep-tagged GCN4-AgrC207 H239Q/ G394A/G396A triple mutant (construct 5). In this case, no pHis signal was associated with the heterodimer, which indicates that cis autophosphorylation cannot occur (Figure 3C, lane 8). Note, the lone pHis band in lane 8 had the same size as construct 4 (see Figure 3C, lane 6), and likely originated from either minor impurities in the preparation or from subunit exchange of the heterodimer (with subsequent autophosphorylation). Collectively, these biochemical experiments suggest that GCN4-AgrC207 strictly autophosphorylates in trans, a result in agreement with previous cell-based complementation studies on full-length AgrC (George Cisar et al., 2009).

#### **Characterization of the DHp-CA Docking Interface**

A distinctive feature of the GCN4-AgrC $_{209}$  structure is the interaction observed between the CA domain of chain A and the DHp  $\alpha 1$  helices from both A and B chains, burying a total surface area of  $\sim\!880$  Å $^2$  (Figure S2A). Importantly, this docked

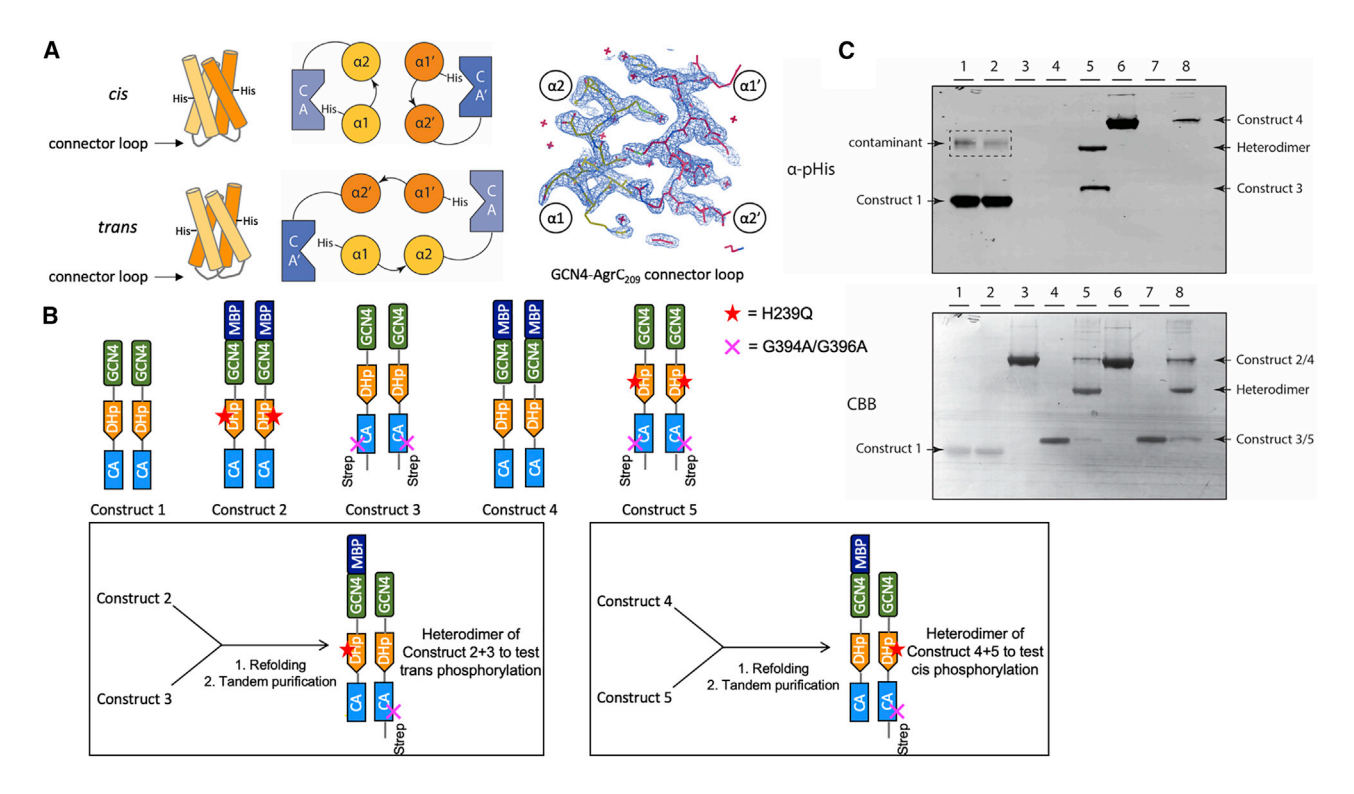


Figure 3. The Autophosphorylation Mode of AgrC

(A) Left: schematic showing the predicted correlation between the handedness of the connector loops within the DHp four-helix bundle and the autophosphorylation mode of the histidine kinase. When viewed from the top of the bundle, the helices are arranged either in a left- or right-handed fashion (and the connector loops are referred to as "left-handed" or "right-handed"), with the former predicted to autophosphorylate in cis and the latter in trans (see text). Right: the  $2F_o-F_c$  map (contoured at  $2.0\sigma$ ) of GCN4-AgrC $_{209}$  focusing on the connector loops in the DHp domain.

(B) Illustration of the constructs used in the in vitro complementation experiment to test the autophosphorylation mode of GCN4-AgrC<sub>207</sub>.

(C) Autophosphorylation assay was performed on indicated GCN4-AgrC<sub>207</sub> homo- or heterodimers and pHis levels were analyzed by immunoblot on a native PAGE gel (top). A CBB-stained western blotting membrane was used as a loading control (bottom). Lane 1, native GCN4-AgrC<sub>207</sub> homodimer (construct 1, see B); lane 2, GCN4-AgrC<sub>207</sub> after denaturation and refolding (construct 1); lane 3, native homodimer of mutant construct 2; lane 4, native homodimer of mutant construct 3: lane 5, refolded heterodimer from mixing constructs 2 and 3: lane 6, native homodimer of construct 4: lane 7, native homodimer of mutant construct 5: lane 8, refolded heterodimer from mixing constructs 4 and 5.

conformation is incompatible with autokinase activity. Given that autophosphorylation of AgrC occurs in trans, we estimate that the  $\gamma$ -phosphorus of ATP bound within the CA domain of chain A is over 30 Å from the N<sup>E</sup> atom of phosphoacceptor His239 of chain B (Figure S2B). Since the GCN4-Agr $C_{209}$  construct has low autokinase activity (Wang et al., 2014a), we postulated that this sequestration was functionally relevant and, by extension, that its disruption would de-repress this inhibition.

Examination of the docking interface reveals two main clusters of electrostatic and H-bonding interactions (Figure 4A). One cluster involves the N-terminal CA α3 helix of chain A and the N-terminal DHp α1 helix of chain B, whereas the second is centered on the C-terminal CA  $\alpha 3$  helix and the H-boxes in the DHp domain. To test the functional importance of these interactions, we performed alanine-scanning mutagenesis on the relevant residues in the context of GCN4-AgrC<sub>209</sub> (Figure 4B and Table S2). This led to the identification of four residues, all within the second cluster, whose mutation resulted in marked enhancement of GCN4-AgrC<sub>209</sub> autophosphorylation over wild-type, namely Arg238, Tyr241, Gln305, and Glu306. Mutation of either Arg238 or Gln305, which are perfectly positioned to form an inter-chain H-bond (Figure 4A), had the most pronounced effect.

Remarkably, the four residues highlighted by the alanine scan were previously identified as mutational hotspots in an unbiased cell-based genetic screen for constitutive AgrC-I mutants (Geisinger et al., 2009). With this in mind, we were keen to see whether mutation of these residues to alanine would directly activate full-length AgrC-I in vitro. For this we expressed and purified the requisite AgrC-I mutants, and reconstituted them into lipid nanodiscs (Figure S3A) (Wang et al., 2014a). Subsequent autophosphorylation assays revealed that the R238A and Q305A mutants had a significantly elevated autokinase activity compared with the wild-type, whereas mutation of Tyr241 or Glu306 had a more modest effect (Figure 4C). This trend is consistent with the results using the GCN4-AgrC<sub>209</sub> construct. The reconstituted system afforded us the opportunity to study the effect of adding AIP ligands to the interface mutants. This revealed that the R238A, Q305A, and Y241A mutants are insensitive to the presence of agonist (AIP-I) or inverse agonist (AIP-II), whereas the E306A mutant behaved similarly to the wild-type receptor. The R238A and Q305A mutants, in particular, have similar levels of activity in the apo state as wild-type AgrC-I has in the agonist bound state. We note that the Q305A mutant is still able to bind tightly to the AIP-I agonist (Figure 6C, see

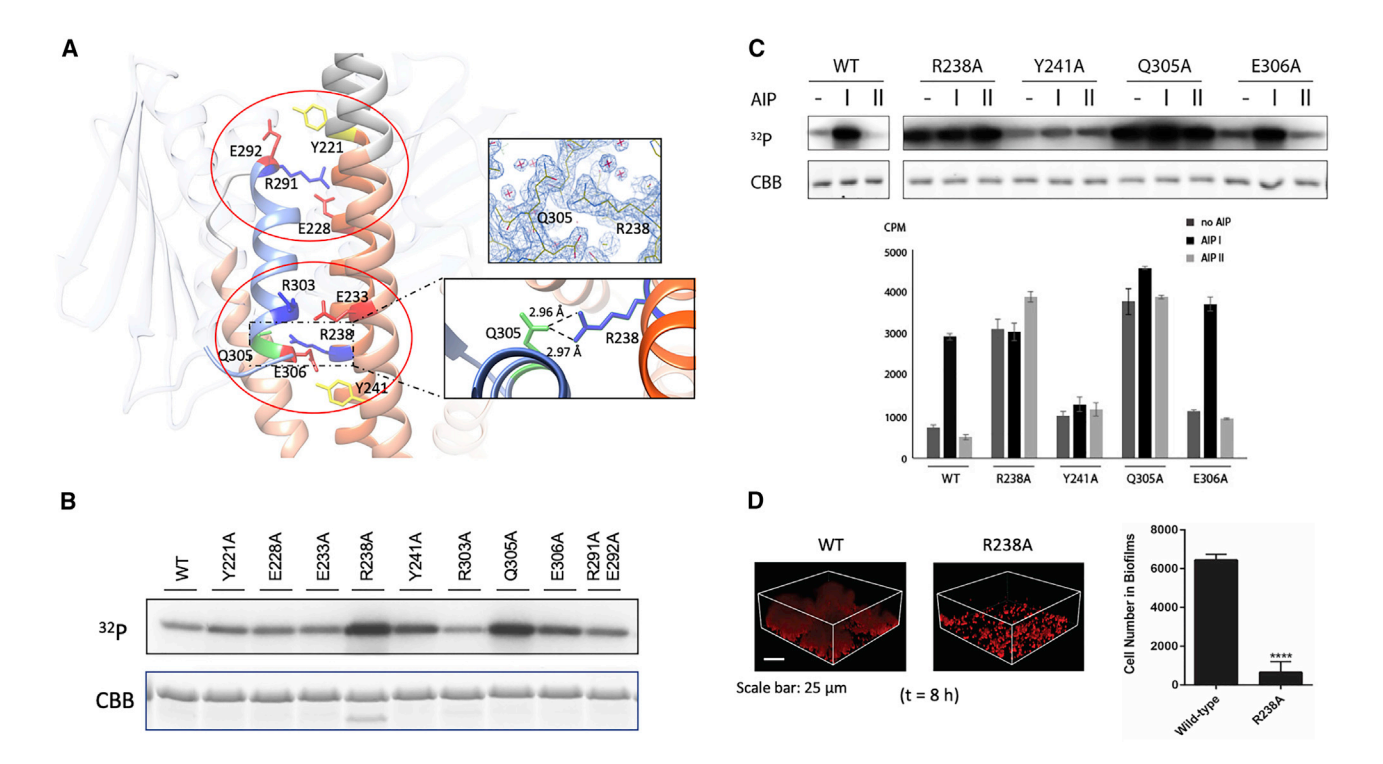


Figure 4. Mapping the Key Residues Involved in the Inhibitory DHp-CA Docking Interaction in AgrC

(A) Close-up view of the docking interface between the DHp and CA domains captured in GCN4-Agr $C_{209}$  structure. Residues that appear to be involved in the docking interaction fall into two clusters, encircled in red. The insets highlight the hydrogen bond formed between Arg238 of chain B and Gln305 of chain A and the  $2F_o - F_c$  map (contoured at  $2.0\sigma$ ) showing the electron density of their side chains.

(B) Autophosphorylation assay was performed on wild-type GCN4-AgrC<sub>209</sub> and indicated alanine mutants and analyzed by autoradiography (top). A CBB-stained SDS-PAGE gel was used as a loading control (bottom).

(C) Full-length wild-type AgrC-I and the selected alanine mutants thereof were assembled into lipid nanodiscs, as described in the STAR Methods. An autophosphorylation assay was performed on purified nanodiscs with AIP peptide included as indicated. Autokinase activity level was either visualized by autoradiography (top) or quantified by scintillation counting and shown as the counts per minute (CPM) value in the bar graph (bottom). Error bars = SD (n = 3).

(D) The biofilm of *S. aureus* cells carrying either wild-type AgrC-I (wild-type [WT]) or AgrC-I R238A mutant accumulated in the microfluidic chamber after 8 h incubation was imaged by confocal microscopy (left). Scale bar, 25  $\mu$ m. The number of cells encased in biofilms covering a surface area of 100 × 100  $\mu$ m<sup>2</sup> was counted separately for *S. aureus* expressing either the AgrC-I WT or the R238A mutant (right). Error bars = SD (n = 4). \*\*\*\*p  $\leq$  0.0001 for an ANOVA pairwise test.

below). Thus, the R238A and Q305A mutants appear to be fully constitutive *in vitro*.

Next we explored the consequences of disrupting the Arg238-Gln305 interaction in a cellular context. As noted earlier, activation of agr signaling triggers S. aureus biofilm dispersal (Boles and Horswill, 2008). With this in mind, we exploited a recently developed microscopy-based assay for monitoring S. aureus biofilm colonization (Kim et al., 2016) (Figure S2C). We introduced either the wild-type agr-I gene cassette or the agr-I gene cassette carrying an R238A mutation in agrC into an agrnull S. aureus strain stably expressing the red fluorescent protein mKate2. To initiate the experiment, equal numbers of cells were separately seeded in microfluidic flow chambers to allow for surface attachment. Planktonic cells were then removed by continually flowing sterile medium through the chamber. At this point (t = 0 h), equal numbers of cells were found to be attached to each chamber as indicated by confocal microscopy (Figure S2D). The chambers were incubated for a further 8 h, and the number of cells in each biofilm matrix was re-counted. This revealed that S. aureus cells carrying the R238A mutation in agrC-I gene had a  $\sim$ 90% reduction in biofilm coverage compared with those carrying wild-type agrC-I (Figure 4D). Hence, disrupting the Arg238-Gln305 H-bond in AgrC is enough to turn on agr signaling and influence the physiology of S. aureus cells.

### The DHp-CA Interface Is Disrupted upon Kinase Activation

Our structural and biochemical data suggest an AgrC activation mechanism in which the CA domain is released from an otherwise sequestered and inactive conformation. We developed a biochemical approach to test this model. Guided by the GCN4-AgrC<sub>209</sub> structure, we identified a residue, Ala299, buried in the DHp-CA interface that is predicted to become more solvent exposed upon HK activation (Figure 5A). By mutating Ala299 to cysteine, it should be possible to probe the status of DHp-CA association by reacting the proteins with a bulky cysteine-reactive electrophile, such as PEG5K-maleimide. The A299C mutation was incorporated into a series of GCN4-HK fusion constructs, each corresponding to a different activity state (Table S2). Note that for the purpose of this study, the sole native cysteine within the CA domain, Cys371, was mutated to serine. Importantly, the GCN4-HK fusions harboring these cysteine mutations retained the same trend of autokinase activity, albeit at a lower level (Figure 5B). Treatment of the proteins

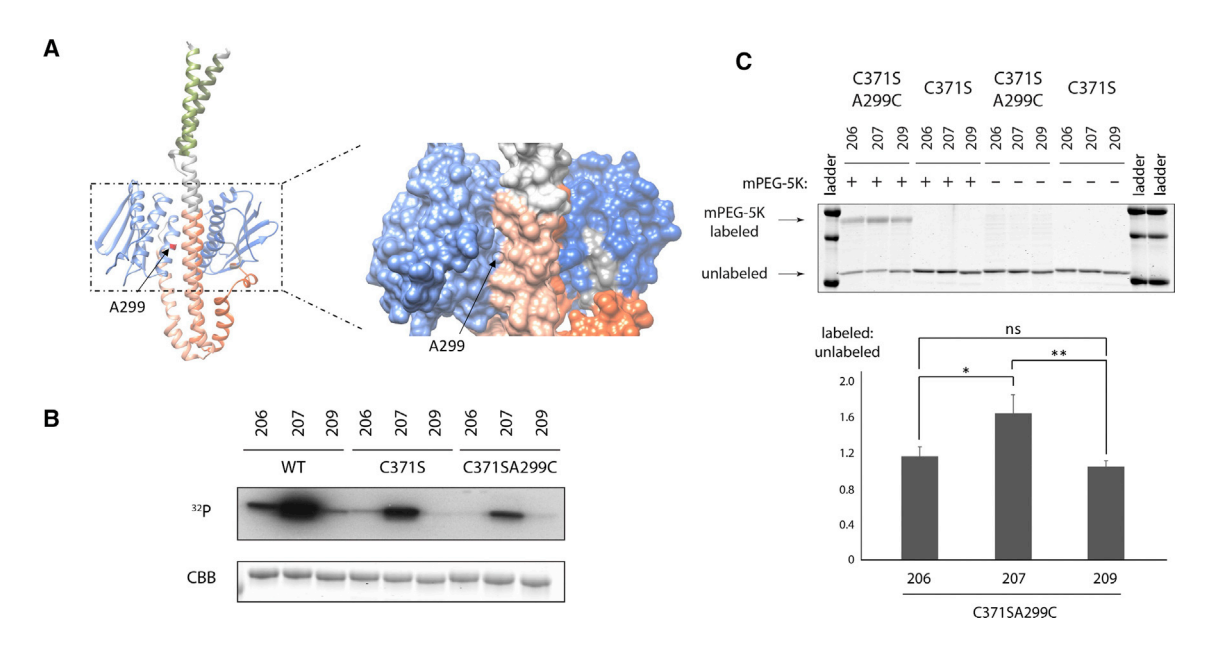


Figure 5. Rotation in the Signaling Helix Regulates the Stability of the DHp-CA Docking Interface

(A) Surface rendering of the GCN4-AgrC<sub>209</sub> structure highlighting the location of Ala299 (red).

(B) Autokinase activities of wild-type GCN4-AgrC<sub>206</sub>, GCN4-AgrC<sub>207</sub>, and GCN4-AgrC<sub>209</sub>, and the mutants harboring either a C371S mutation or C371S/A299C double mutations. Reactions were monitored by autoradiography. A CBB-stained SDS-PAGE gel was used as the loading control.

(C) Cysteine accessibility assay. Indicated GCN4 chimeras were reacted with PEG5K-maleimide and analyzed by SDS-PAGE gel (top). The intensity of protein bands corresponding to the PEG5K-maleimide-labeled species and the unlabeled species was individually quantified by densitometry and the ratio of the two was reported as a measure of the labeling efficiency at the Ala299 position (bottom). Error bars = SD (n = 3). \*p  $\leq$  0.05; \*\*p  $\leq$  0.01; n.s., not significant, p > 0.05 for an unpaired Student's t test.

with PEG5K-maleimide revealed clear differences in cysteine reactivity (Figure 5C). The construct with the fusion junction at AgrC residue 207, which had the highest autokinase activity, was most efficiently labeled at A299C. In contrast, the least-active construct (with the fusion junction at residue 209) showed the lowest level of labeling. The observed correlation between HK activity and the Ala299 accessibility supports the model that the DHp-CA docking interface is disrupted as part of AgrC activation. Efforts to include GCN4-HK fusion constructs containing Q305A in the background of C371S/A299C for a parallel comparison were not successful due to poor expression.

#### Structural Consequences of Disrupting the Arg238-Gln305 Interaction

We next investigated whether breaking the Arg238-Gln305 H-bond at the DHp-CA docking interface has any effect on the conformation of the S helix in full-length AgrC. An inter-chain disulfide crosslinking strategy was employed for this purpose in which a cysteine mutation was incorporated at residues 205–209 in the S helix. We have previously shown that the S helix conformation can be deduced from the extent of disulfide-linked dimer obtained as a function of cysteine position (Wang et al., 2014a). For this analysis, we elected to focus on the Q305A mutation so as to avoid direct perturbation on the DHp helices.

The requisite cysteine mutations were introduced into both wild-type AgrC-I and the Q305A mutant background. These proteins were expressed, purified, and incorporated into nanodiscs (Figure S3B). Reconstituted proteins were then treated with oxidized glutathione in the presence or absence of AIPs, resolved on a non-reducing SDS-PAGE gel and the amount of

the crosslinked dimer was quantified by densitometry (Figures 6A and 6B). Although wild-type AgrC-I contains two native cysteines (Cys91 in the sensor and Cys371 in the CA), they produced little crosslinking background. Hence, the amount of covalent dimer formed in the mutants reflects the propensity of the cysteine pair exogenously introduced to form an inter-chain disulfide. The crosslinking pattern observed for the Q305A mutant in the presence of AIP-I was nearly identical to that of the wild-type receptor under the same condition (Figures 6A and 6B). By contrast, for the apo form and the AIP-II bound form, crosslinking at residue positions 206 and 209 increased while crosslinking at residue positions 205 and 208 slightly decreased when compared with the wild-type. As a consequence, the crosslinking pattern obtained for the Q305A mutant in both the apo and AIP-II bound forms seems to shift toward that associated with the active state, as represented by the AIP-I bound form. This indicates that disruption of the Arg238-Gln305 interaction alters the conformational equilibrium of the S helix.

We next explored whether the conformational change in the AgrC-I S helix induced by the Q305A mutation propagates across the membrane and affects AIP ligand binding. Using a fluorescence anisotropy assay in which a fluorescein-labeled AIP-I analog (FAM-AIP-I) is displaced from the AgrC nanodiscs by unlabeled AIP (Wang et al., 2014a), we measured the dissociation constants (K<sub>d</sub>) of AIP-I/II for the Q305A mutant receptor (Figures 6C and S4) and compared this with the previously reported values for the wild-type AgrC-I. This revealed that the constitutive mutation does not significantly change AIP-I binding: the  $K_{\rm d}$  for the mutant receptor was  $56.0\pm11.2$  nM compared

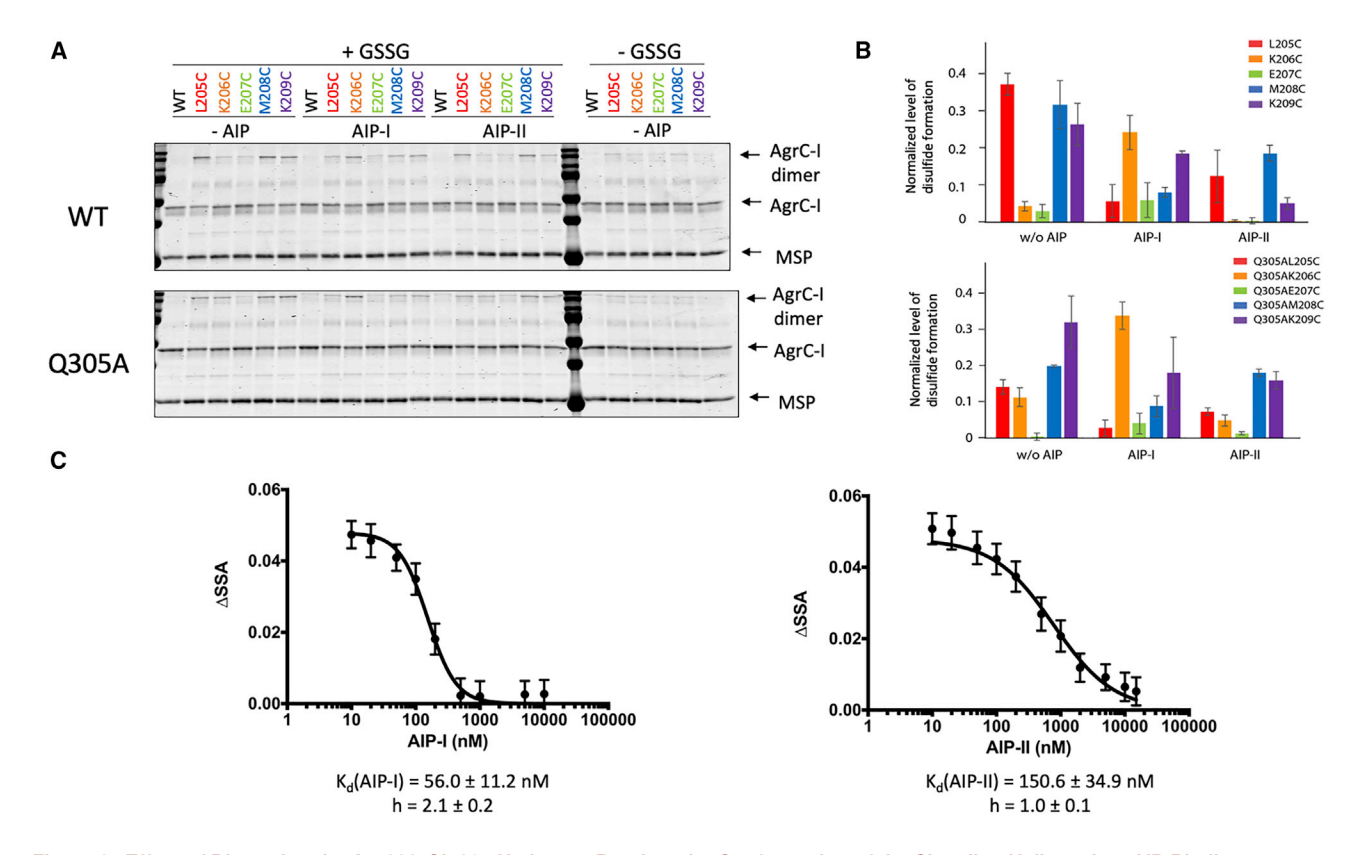


Figure 6. Effect of Disrupting the Arg238-Gln305 Hydrogen Bond on the Conformation of the Signaling Helix and on AIP Binding (A) Five single cysteine point mutations were individually introduced into the S helix of either the full-length AgrC-I WT or the Q305A mutant. The purified proteins were assembled into lipid nanodiscs, disulfide crosslinked under three different ligand states (no AIP, with AIP-I, or with AIP-II) and analyzed by SDS-PAGE as indicated

(B) Quantification of the extent of crosslinking for each AgrC-I cysteine mutant (color coded), with the intensity of the crosslinked dimer band determined by densitometry normalized against that of the membrane scaffold protein (MSP). Error bars = SD (n = 3). The crosslinking pattern under three different ligand states was compared between AgrC-I WT (top) and the Q305A mutant (bottom).

(C) AIP-I (left panel) or AIP-II (right panel) was titrated into a pre-formed complex of AgrC-I Q305A nanodiscs and FAM-AIP-I. Competitive displacement of FAM-AIP-I was monitored by steady-state anisotropy change (ΔSSA). One representative titration of three is shown. The error bars (technical) show SEM (n = 10).

with 63 ± 13 nM for the wild-type. Similarly, AIP-II bound the mutant receptor with a K<sub>d</sub> of 150.6 ± 34.9 nM, which is again close to that reported for the wild-type AgrC-I (160 ± 20 nM) (Wang et al., 2014a). Interestingly, we did observe a Hill coefficient larger than 1 for AIP-I binding to the Q305A mutant (h =  $2.1 \pm 0.2$ ), in contrast to the wild-type (Wang et al., 2014a). It is unclear how (or if) this relates to the aforementioned conformational changes in the S helix. Overall, these binding studies imply that disruption of the Arg238-Gln-305 interaction has a structural effect more localized to the AgrC HK module, which is not transmitted to the AIP binding pocket in the sensor domain.

#### **DISCUSSION**

We have described the crystal structure of the complete cytoplasmic region of S. aureus AgrC-I, a member of the group 10 histidine protein kinase (HPK<sub>10</sub>) subfamily that is prevalent in the Firmicutes phylum of bacteria (Wang et al., 2014a). The crystallization construct employed, GCN4-AgrC<sub>209</sub>, functionally mimicks the apo form of the receptor (Wang et al., 2014a). Our structure captured a conformation where the CA domain of one protomer is docked onto the two DHp  $\alpha$ 1 helices in the homodimer. This sequesters the CA domain from the histidine autophosphorylation site, thereby offering a structural explanation for the low autokinase activity of the construct. Structureguided mutagenesis confirmed that this docking interaction suppresses the autokinase activity of AgrC-I, and, moreover, revealed that a hydrogen-bonding interaction between residues Arg238 and Gln305 is critical for this mode of regulation. Collectively, our biochemical studies are consistent with a model for AgrC-I activation in which binding of the AIP-I agonist alters the conformation of the S helix that propagates down the DHp coiled coil and breaks the H-bond between Gln305 and Arg238 (Figure S6A). The CA domain is thus released from its sequestered state and at the same time His239 becomes more accessible to phosphorylation. Conceivably, additional structural changes within the HK are associated with engagement of the newly unleashed CA domain with the histidine on the other protomer to form the Michaelis complex. The nature of these putative structural reorganizations (including whether deformation of DHp  $\alpha$ 2 helix is involved) remains to be explored.

The GCN4-AgrC<sub>209</sub> example adds to a growing list of HK structures in which a DHp-CA docking interaction is observed. Other examples include HK853 from T. maritima (Marina et al.,

2005) (PDB: 2C2A), DesK from *B. subtilis* (Albanesi et al., 2009) (PDB: 3EHH and 3EHJ), VicK from *S. mutans* (Wang et al., 2013) (PDB: 4I5S), and CpxA from *E. coli* (Mechaly et al., 2014) (PDB: 4BIV). While the precise details of the DHp-CA docking site differ from case to case—including whether hydrophobic or hydrophilic contacts dominate the interface and to what extent the "Gripper" helix in the CA domain is involved (Bhate et al., 2015) (Figure S5A)—a unifying theme does emerge from this body of structural work, namely the idea that the kinase activity of the HK module is regulated through controlling the proximity of the CA domain with respect to the phosphoacceptor histidine.

There is a remarkable level of concordance between the structural data presented here and the results from a previous genetic screen to identify constitutive AgrC mutants (Geisinger et al., 2009). All of the constitutive mutations discovered in the HK module localize to the docking interface identified in this study (Figure S5B). Moreover, residues Arg238 and Gln305 were found to be mutational hotspots. The structural basis of this observation is now clear: Arg238 and Gln305 directly engage in an inter-chain H-bond that is critical to CA domain sequestration. Interestingly, a recent study reported that a single Y223C mutation in AgrC is capable of switching a cytotoxic methicillin-resistant S. aureus (MRSA) strain to a colonizing phenotype, while the reverse mutation C223Y in an AgrC variant from another colonizing MRSA strain switches it to a cytotoxic profile (Mairpady Shambat et al., 2016). The authors attributed this phenotypic switch to an altered binding affinity between AgrC and AgrA. Visual examination of our GCN4-AgrC<sub>209</sub> structure indicates that Tyr223 also locates at the DHp-CA interface, suggesting that Y223C in AgrC might stabilize the inhibitory docking interaction and thus repress agr signaling.

Sequence analysis reveals that the Arg238-Gln305 pair is invariant in AgrC orthologs across Staphylococceae (Figure S6B). Extending this analysis to the broader HPK<sub>10</sub> subfamily, which includes AgrC and a number of other RHKs that respond to peptide pheromones, reveals that either an Arg or a Lys is always present at the position corresponding to Arg238. At the position equivalent to Gln305, a Gln or Asn residue is highly enriched (32.5%) compared with the combined frequency of Gln and Asn (~4% each) in eubacterial proteins (Pe'er et al., 2004) (Figure S6B; Table S3). By contrast, the conserved Arg238-Gln305 pair (or its equivalent) is not present among more distant members of the histidine protein kinase family such as the aforementioned HK853, DesK, and VicK (Figure S6B). Based on this, we propose that a DHp-CA docking interaction analogous to that seen in AgrC-I evolved among a subset of HPK<sub>10</sub> family members and that, by extension, a similar mode of autokinase regulation may also be operational in these cases.

The ability of AIPs from different *agr* specificity groups to either activate or inhibit AgrC represents a unique feature of this QS system. *Agr* interference is thought to account for why individual clinical isolates of *S. aureus* are typically homogeneous with respect to the *agr* genotype (Jarraud et al., 2002). At the molecular level, how can one understand this type of agonism versus inverse agonism behavior? Based on the available structural and biochemical data, it seems clear that different activity states of AgrC are driven by ligand-induced structural changes in the

sensor domain that ultimately result in differential conformations in the S helix/DHp. While the mechanism(s) by which ligand binding induces these structural changes has yet been resolved, some clues can be gleaned from the aforementioned genetic screen that resulted in constitutive mutants of AgrC (Geisinger et al., 2009). In addition to the activating mutations mapped to the DHp-CA interface, we also observed mutations within the predicted last helix of the sensor domain, which is directly linked to the S helix (Figure S5B). Mutations elsewhere in the sensor were not identified. Based on this observation, it seems likely that structural changes induced by AIP binding propagate through this region of the sensor to the S helix. Studies on other RHKs have led to competing models of transmembrane signaling upon sensor activation (Sevvana et al., 2008; Molnar et al., 2014; Neiditch et al., 2006). These include piston-like conformational changes, as well as various scissor-like and rotational-type motions. Importantly, many of these sensor kinases contain additional domains (such as HAMP or PAS) sandwiched between the transmembrane domain and the HK module. These domains can act to amplify and/or convert motions emanating from the transmembrane domain into conformational changes in the HK. For example, structural studies on the E. coli nitrate/ nitrite sensor, NarQ, indicated that the HAMP domain converts piston-like motions in the transmembrane domain to rotational motions that propagate into the HK (Gushchin et al., 2017). AgrC, like other HPK<sub>10</sub> subfamily members, does not contain an "amplifier/converter" such as a HAMP domain; rather the S helix is directly linked to the sensor. Consequently, it is difficult to imagine how a transduction mechanism analogous to NarQ could be operational in AgrC. Instead, we propose that AIP binding stabilizes (or conceivably induces) discrete rotational conformations in the last helix of the sensor that are directly transduced by the S helix into the DHp domain. Ultimately, high-resolution structural information on the receptor in complex with AIPs will be needed to test this idea.

In conclusion, we have elucidated a key hydrogen bond in the HK module of AgrC that is critical for regulation of autokinase activity. Our data are consistent with the idea that mechanical motions induced by ligand binding in the sensor either disrupt (in the case of agonists) or stabilize (inverse agonists) this inhibitory interaction, resulting in elevated or diminished autokinase activity relative to the apo form of the receptor. As such, our study provides a conceptual advance in understanding the mechanism of signal transduction in this pharmacologically important RHK.

#### **SIGNIFICANCE**

The receptor histidine kinase AgrC is part of a two-component system in S. aureus that regulates virulence of the pathogen based on bacterial quorum. In this study, we report the structure of an AgrC chimera that harbors the full cytoplasmic histidine kinase module with an N-terminal GCN4 coiled-coil fusion. The structure captures AgrC in the "off" state, one in which inter-domain contacts stabilize a sequestered conformation of the catalytic domain incompatible with autophosphorylation. Mutagenesis studies pinpoint a key H-bonding interaction, between Arg238 and Gln305, which acts as a "latch" to stabilize this sequestered state. Based on biochemical studies, we propose that this

interaction is regulated by structural changes that propagate from ligand binding in the sensor domain to the kinase module. Collectively, this study takes us one step closer to a complete understanding of signal transduction through AgrC, and reveals a protein interface that potentially could be targeted pharmacologically for controlling *S. aureus* virulence and biofilm formation.

#### **STAR**\*METHODS

Detailed methods are provided in the online version of this paper and include the following:

- KEY RESOURCES TABLE
- CONTACT FOR REAGENT AND RESOURCE SHARING
- EXPERIMENTAL MODEL AND SUBJECT DETAILS
  - Bacterial Strains
- METHOD DETAILS
  - O Protein Production and Nanodisc Assembly
  - O Crystallization and Structure Determination
  - Autokinase Assays
  - O Cysteine Accessibility Assay
  - O Cysteine Crosslinking of AgrC-I Nanodisc
  - Fluorescence Anisotropy-Based Binding Assay
  - Biofilm Analysis by Microscope Imaging
- QUANTIFICATION AND STATISTICAL ANALYSIS
- DATA AND SOFTWARE AVAILABILITY
  - Data Resources

#### SUPPLEMENTAL INFORMATION

Supplemental Information includes six figures and three tables and can be found with this article online at https://doi.org/10.1016/j.chembiol.2019. 01.006.

#### **ACKNOWLEDGMENTS**

The authors would like to acknowledge members of the Muir Group for valuable discussions. This work was based on research conducted at Cornell High Energy Synchrotron Source (CHESS), which is supported by the NSF award DMR-1332208, and the MacCHESS, which is supported by NIGMS award GM-103485. This work was supported by NIH grants Al042783 and GM095880

#### **AUTHOR CONTRIBUTIONS**

Q.X. and T.W.M. designed the experiments. Q.X., A.Z., and M.K.K. performed the experiments. Q.X., A.Z., M.K.K. and T.W.M. analyzed the data. Q.X. and P.D.J. solved the crystal structures. Q.X., A.Z., and T.W.M. wrote the manuscript. B.L.B., H.A.S., R.P.N., and T.W.M. supervised the project.

#### **DECLARATION OF INTERESTS**

The authors declare no competing interest.

Received: June 4, 2018 Revised: November 27, 2018 Accepted: January 10, 2019 Published: February 14, 2019

#### **SUPPORTING CITATIONS**

The following references appear in the Supplemental Information: Wang et al., 2014b.

#### REFERENCES

Adams, P.D., Afonine, P.V., Bunkoczi, G., Chen, V.B., Davis, I.W., Echols, N., Headd, J.J., Hung, L.W., Kapral, G.J., Grosse-Kunstleve, R.W., et al. (2010). PHENIX: a comprehensive Python-based system for macromolecular structure solution. Acta Crystallogr. D Biol. Crystallogr. 66, 213–221.

Albanesi, D., Martin, M., Trajtenberg, F., Mansilla, M.C., Haouz, A., Alzari, P.M., de Mendoza, D., and Buschiazzo, A. (2009). Structural plasticity and catalysis regulation of a thermosensor histidine kinase. Proc. Natl. Acad. Sci. U S A *106*, 16185–16190.

Ashenberg, O., Keating, A.E., and Laub, M.T. (2013). Helix bundle loops determine whether histidine kinases autophosphorylate in *cis* or in *trans*. J. Mol. Biol. *425*. 1198–1209.

Berntsson, O., Diensthuber, R.P., Panman, M.R., Bjorling, A., Gustavsson, E., Hoernke, M., Hughes, A.J., Henry, L., Niebling, S., Takala, H., et al. (2017). Sequential conformational transitions and alpha-helical supercoiling regulate a sensor histidine kinase. Nat. Commun. 8, 284.

Bhate, M.P., Molnar, K.S., Goulian, M., and Degrado, W.F. (2015). Signal transduction in histidine kinases: insights from new structures. Structure *23*, 981–994.

Boles, B.R., and Horswill, A.R. (2008). Agr-mediated dispersal of *Staphylococcus aureus* biofilms. PLoS Pathog. 4, e1000052.

Capra, E.J., and Laub, M.T. (2012). Evolution of two-component signal transduction systems. Annu. Rev. Microbiol. 66, 325–347.

Casino, P., Miguel-Romero, L., and Marina, A. (2014). Visualizing autophosphorylation in histidine kinases. Nat. Commun. 5, 3258.

Casino, P., Rubio, V., and Marina, A. (2009). Structural insight into partner specificity and phosphoryl transfer in two-component signal transduction. Cell 139, 325–336.

Dago, A.E., Schug, A., Procaccini, A., Hoch, J.A., Weigt, M., and Szurmant, H. (2012). Structural basis of histidine kinase autophosphorylation deduced by integrating genomics, molecular dynamics, and mutagenesis. Proc. Natl. Acad. Sci. U S A 109, E1733–E1742.

Diensthuber, R.P., Bommer, M., Gleichmann, T., and Moglich, A. (2013). Full-length structure of a sensor histidine kinase pinpoints coaxial coiled coils as signal transducers and modulators. Structure *21*, 1127–1136.

Dufour, P., Jarraud, S., Vandenesch, F., Greenland, T., Novick, R.P., Bes, M., Etienne, J., and Lina, G. (2002). High genetic variability of the agr locus in *Staphylococcus* species. J. Bacteriol. *184*, 1180–1186.

Dutta, R., and Inouye, M. (2000). GHKL, an emergent ATPase/kinase superfamily. Trends Biochem. Sci. 25, 24–28.

Emsley, P., Lohkamp, B., Scott, W.G., and Cowtan, K. (2010). Features and development of Coot. Acta Crystallogr. D Biol. Crystallogr. 66, 486–501.

Ferris, H.U., Coles, M., Lupas, A.N., and Hartmann, M.D. (2014). Crystallographic snapshot of the *Escherichia coli* EnvZ histidine kinase in an active conformation. J. Struct. Biol. *186*, 376–379.

Ferris, H.U., Dunin-Horkawicz, S., Hornig, N., Hulko, M., Martin, J., Schultz, J.E., Zeth, K., Lupas, A.N., and Coles, M. (2012). Mechanism of regulation of receptor histidine kinases. Structure *20*, 56–66.

Geisinger, E., Muir, T.W., and Novick, R.P. (2009). Agr receptor mutants reveal distinct modes of inhibition by staphylococcal autoinducing peptides. Proc. Natl. Acad. Sci. U S A *106*. 1216–1221.

George Cisar, E.A., Geisinger, E., Muir, T.W., and Novick, R.P. (2009). Symmetric signalling within asymmetric dimers of the *Staphylococcus aureus* receptor histidine kinase AgrC. Mol. Microbiol. *74*, 44–57.

Gordon, C.P., Williams, P., and Chan, W.C. (2013). Attenuating *Staphylococcus aureus* virulence gene regulation: a medicinal chemistry perspective. J. Med. Chem. *56*, 1389–1404.

Gushchin, I., Melnikov, I., Polovinkin, V., Ishchenko, A., Yuzhakova, A., Buslaev, P., Bourenkov, G., Grudinin, S., Round, E., Balandin, T., et al. (2017). Mechanism of transmembrane signaling by sensor histidine kinases. Science 356, https://doi.org/10.1126/science.aah6345.

Jarraud, S., Mougel, C., Thioulouse, J., Lina, G., Meugnier, H., Forey, F., Nesme, X., Etienne, J., and Vandenesch, F. (2002). Relationships between

Staphylococcus aureus genetic background, virulence factors, agr groups (alleles), and human disease. Infect. Immun. 70, 631-641.

Ji, G., Beavis, R., and Novick, R.P. (1997). Bacterial interference caused by autoinducing peptide variants. Science 276, 2027-2030.

Johnson, J.G., Wang, B., Debelouchina, G.T., Novick, R.P., and Muir, T.W. (2015). Increasing AIP macrocycle size reveals key features of agr activation in Staphylococcus aureus. Chembiochem 16, 1093-1100.

Kee, J.M., Oslund, R.C., Perlman, D.H., and Muir, T.W. (2013). A pan-specific antibody for direct detection of protein histidine phosphorylation. Nat. Chem. Biol. 9. 416-421.

Kim, M.K., Ingremeau, F., Zhao, A., Bassler, B.L., and Stone, H.A. (2016). Local and global consequences of flow on bacterial quorum sensing. Nat. Microbiol. 1, 15005.

Kim, M.K., Zhao, A., Wang, A., Brown, Z.Z., Muir, T.W., Stone, H.A., and Bassler, B.L. (2017). Surface-attached molecules control Staphylococcus aureus quorum sensing and biofilm development. Nat. Microbiol. 2, 17080.

Kong, K.F., Vuong, C., and Otto, M. (2006). Staphylococcus quorum sensing in biofilm formation and infection. Int. J. Med. Microbiol. 296, 133-139.

Lyon, G.J., Mayville, P., Muir, T.W., and Novick, R.P. (2000). Rational design of a global inhibitor of the virulence response in Staphylococcus aureus, based in part on localization of the site of inhibition to the receptor-histidine kinase, AgrC. Proc. Natl. Acad. Sci. U S A 97, 13330-13335.

Lyon, G.J., Wright, J.S., Muir, T.W., and Novick, R.P. (2002). Key determinants of receptor activation in the agr autoinducing peptides of Staphylococcus aureus. Biochemistry 41, 10095-10104.

Mairpady Shambat, S., Siemens, N., Monk, I.R., Mohan, D.B., Mukundan, S., Krishnan, K.C., Prabhakara, S., Snall, J., Kearns, A., Vandenesch, F., et al. (2016). A point mutation in AgrC determines cytotoxic or colonizing properties associated with phenotypic variants of ST22 MRSA strains. Sci. Rep. 6, 31360.

Marina, A., Waldburger, C.D., and Hendrickson, W.A. (2005). Structure of the entire cytoplasmic portion of a sensor histidine-kinase protein. EMBO J. 24,

Mayville, P., Ji, G., Beavis, R., Yang, H., Goger, M., Novick, R.P., and Muir, T.W. (1999). Structure-activity analysis of synthetic autoinducing thiolactone peptides from Staphylococcus aureus responsible for virulence. Proc. Natl. Acad. Sci. U S A 96. 1218-1223.

McCoy, A.J., Grosse-Kunstleve, R.W., Adams, P.D., Winn, M.D., Storoni, L.C., and Read, R.J. (2007). Phaser crystallographic software. J. Appl. Crystallogr.

Mechaly, A.E., Sassoon, N., Betton, J.M., and Alzari, P.M. (2014). Segmental helical motions and dynamical asymmetry modulate histidine kinase autophosphorylation. PLoS Biol. 12, e1001776.

Molnar, K.S., Bonomi, M., Pellarin, R., Clinthorne, G.D., Gonzalez, G., Goldberg, S.D., Goulian, M., Sali, A., and Degrado, W.F. (2014). Cys-scanning disulfide crosslinking and Bayesian modeling probe the transmembrane signaling mechanism of the histidine kinase, PhoQ. Structure 22, 1239-1251.

Murshudov, G.N., Skubak, P., Lebedev, A.A., Pannu, N.S., Steiner, R.A., Nicholls, R.A., Winn, M.D., Long, F., and Vagin, A.A. (2011). REFMAC5 for the refinement of macromolecular crystal structures. Acta Crystallogr. D Biol. Crystallogr. 67, 355-367.

Neiditch, M.B., Federle, M.J., Pompeani, A.J., Kelly, R.C., Swem, D.L., Jeffrey, P.D., Bassler, B.L., and Hughson, F.M. (2006). Ligand-induced asymmetry in histidine sensor kinase complex regulates quorum sensing. Cell 126,

Novick, R.P., Projan, S.J., Kornblum, J., Ross, H.F., Ji, G., Kreiswirth, B., Vandenesch, F., and Moghazeh, S. (1995). The agr P2 operon: an autocatalytic sensory transduction system in Staphylococcus aureus. Mol. Gen. Genet. 248,

Novick, R.P., Ross, H.F., Projan, S.J., Kornblum, J., Kreiswirth, B., and Moghazeh, S. (1993). Synthesis of staphylococcal virulence factors is controlled by a regulatory RNA molecule. EMBO J. 12, 3967-3975.

Pe'er, I., Felder, C.E., Man, O., Silman, I., Sussman, J.L., and Beckmann, J.S. (2004). Proteomic signatures: amino acid and oligopeptide compositions differentiate among phyla. Proteins 54, 20-40.

Pettersen, E.F., Goddard, T.D., Huang, C.C., Couch, G.S., Greenblatt, D.M., Meng, E.C., and Ferrin, T.E. (2004). UCSF Chimera - a visualization system for exploratory research and analysis. J. Comput. Chem. 25, 1605-1612.

Ritchie, T.K., Grinkova, Y.V., Bayburt, T.H., Denisov, I.G., Zolnerciks, J.K., Atkins, W.M., and Sligar, S.G. (2009). Reconstitution of membrane proteins in phospholipid bilayer nanodiscs. Methods Enzymol. 464, 211-231.

Sevvana, M., Vijayan, V., Zweckstetter, M., Reinelt, S., Madden, D.R., Herbst-Irmer, R., Sheldrick, G.M., Bott, M., Griesinger, C., and Becker, S. (2008). A ligand-induced switch in the periplasmic domain of sensor histidine kinase CitA. J. Mol. Biol. 377, 512-523.

Sidote, D.J., Barbieri, C.M., Wu, T., and Stock, A.M. (2008). Structure of the Staphylococcus aureus AgrA LytTR domain bound to DNA reveals a beta fold with an unusual mode of binding. Structure 16, 727-735.

Srivastava, S.K., Rajasree, K., Fasim, A., Arakere, G., and Gopal, B. (2014). Influence of the AgrC-AgrA complex on the response time of Staphylococcus aureus quorum sensing. J. Bacteriol. 196, 2876-2888.

Tal-Gan, Y., Stacy, D.M., Foegen, M.K., Koenig, D.W., and Blackwell, H.E. (2013). Highly potent inhibitors of quorum sensing in Staphylococcus aureus revealed through a systematic synthetic study of the group-III autoinducing peptide. J. Am. Chem. Soc. 135, 7869-7882.

Thoendel, M., Kavanaugh, J.S., Flack, C.E., and Horswill, A.R. (2011). Peptide signaling in the staphylococci. Chem. Rev. 111, 117-151.

Tickle, I.J., Flensburg, C., Keller, P., Paciorek, W., Sharff, A., Smart, O., Vonrhein, C., and Bricogne, G. (2018). STARANISO (Global Phasing Ltd). http://staraniso.globalphasing.org/cgi-bin/staraniso.cgi, Accessed 5th. 2018.

Vasquez, J.K., Tal-Gan, Y., Cornilescu, G., Tyler, K.A., and Blackwell, H.E. (2017). Simplified AIP-II peptidomimetics are potent inhibitors of Staphylococcus aureus AgrC quorum sensing receptors. Chembiochem 18, 413-423.

Vuong, C., Saenz, H.L., Gotz, F., and Otto, M. (2000). Impact of the agr quorum-sensing system on adherence to polystyrene in Staphylococcus aureus. J. Infect. Dis. 182, 1688-1693.

Walshaw, J., and Woolfson, D.N. (2001). Socket: a program for identifying and analysing coiled-coil motifs within protein structures. J. Mol. Biol. 307, 1427-1450.

Wang, B., and Muir, T.W. (2016). Regulation of virulence in Staphylococcus aureus: molecular mechanisms and remaining puzzles. Cell Chem. Biol. 23,

Wang, B., Zhao, A., Novick, R.P., and Muir, T.W. (2014a), Activation and inhibition of the receptor histidine kinase AgrC occurs through opposite helical transduction motions. Mol. Cell 53, 929-940.

Wang, B., Zhao, A., Xie, Q., Olinares, P.D., Chait, B.T., Novick, R.P., and Muir, T.W. (2017). Functional plasticity of the AgrC receptor histidine kinase required for staphylococcal virulence. Cell Chem. Biol. 24, 76-86.

Wang, C., Sang, J., Wang, J., Su, M., Downey, J.S., Wu, Q., Wang, S., Cai, Y., Xu, X., Wu, J., et al. (2013). Mechanistic insights revealed by the crystal structure of a histidine kinase with signal transducer and sensor domains. PLoS Biol. 11, e1001493.

Wang, L., Quan, C., Xiong, W., Qu, X., Fan, S., and Hu, W. (2014b). New insight into transmembrane topology of Staphylococcus aureus histidine kinase AgrC. Biochim. Biophys. Acta 1838, 988-993.

Wright, J.S., 3rd, Jin, R., and Novick, R.P. (2005). Transient interference with staphylococcal quorum sensing blocks abscess formation. Proc. Natl. Acad. Sci. U S A 102, 1691-1696.

Zhang, L., Gray, L., Novick, R.P., and Ji, G. (2002). Transmembrane topology of AgrB, the protein involved in the post-translational modification of AgrD in Staphylococcus aureus. J. Biol. Chem. 277, 34736-34742.

#### **STAR**\*METHODS

#### **KEY RESOURCES TABLE**

Antibodies Rabbit anti-pHis polyclonal antibody (Kee et al., 2013) N/A  Bacterial and Virus Strains Staphylococcus aureus strain RN4220 Richard Novick N/A  Staphylococcus aureus strain RN9011 Richard Novick N/A  Staphylococcus aureus strain RN9011 Richard Novick N/A  Staphylococcus aureus strain RN9011 Richard Novick N/A  Staphylococcus aureus strain RN7206 Richard Novick N/A  Staphylococcus aureus strain RN7206 Richard Novick N/A  Biological Samples Plasmid for membrane scaffold protein MSP1E3D1 Addgene #20066 site-specific integration suicide vector pJC1111 Richard Novick N/A  Chemicals, Peptides, and Recombinant Proteins FAM-AIP-I Tom Muir; (Lyon et al., 2002) N/A  Deposited Data Structure of GCN4-AgrC200 fusion chimera (anisotropic cutoff) this paper Protein Data Bank accession code: 6E52 Structure of AgrC CA domain (Srivastava et al., 2014) Protein Data Bank accession code: 4BXI Structure of EnvZ HK chimera with the DHp connector loop of HK853 Structure of PCXA HK module with ATP bound (Mechaly et al., 2014) Protein Data Bank accession code: 4BIV Structure of Desk HK module H188V mutant in complex (Marina et al., 2005) Richard Novick N/A  Chemicals, Peptides, and Recombinant Proteins Richard Novick N/A  Chemicals, Peptides, and Recombinant Proteins Richard Novick N/A  Chemicals, Peptides, and Recombinant Proteins Richard Novick N/A  Chemicals, Peptides, and Recombinant Protein MSP18301 Richard Novick N/A  Chemicals, Peptides, and Recombinant Protein MSP18301 Richard Novick N/A  Chemicals, Peptides, and Recombinant Protein MSP18301 Richard Novick N/A  Chemicals, Peptides, and Recombinant Protein MSP18301 Richard Novick N/A  Chemicals Peptides, and Recombinant Protein MSP18301 Richard Novick N/A  Chemicals Peptides, and Recombinant Protein MSP18301 Richard Novick N/A  Chemicals Peptides, and Recombination N/A  Richard Novi			
Rabbit anti-pHis polyclonal antibody (Kee et al., 2013) N/A  Bacterial and Virus Strains  Staphylococcus aureus strain RN4220 Richard Novick N/A  Staphylococcus aureus strain RN9011 Richard Novick N/A  Staphylococcus aureus strain RN9011 Richard Novick N/A  Staphylococcus aureus strain RN7206 Richard Novick N/A  Escherichia coli B834 (DE3) Fred Hughson N/A  Biological Samples  Plasmid for membrane scaffold protein MSP1E3D1 Addgene #20066  site-specific integration suicide vector pJC1111 Richard Novick N/A  Chemicals, Peptides, and Recombinant Proteins  FAM-AIP-1 Tom Muir; (Lyon et al., 2002) N/A  Deposited Data  Structure of GCN4-AgrC <sub>209</sub> fusion chimera (anisotropic cutoff) this paper Protein Data Bank accession code: 6E52  Structure of GCN4-AgrC <sub>209</sub> fusion chimera (isotropic cutoff) this paper Protein Data Bank accession code: 6E95  Structure of AgrC CA domain (Srivastava et al., 2014) Protein Data Bank accession code: 4BXI  Structure of EnvZ HK chimera with the DHp connector loop of HK853  Structure of CPXA HK module with ATP bound (Mechaly et al., 2014) Protein Data Bank accession code: 4BIV  Structure of PoxA HK module with ATP bound (Mechaly et al., 2014) Protein Data Bank accession code: 2C2A  Structure of DesK HK module H188V mutant in complex (Albanesi et al., 2005) Protein Data Bank accession code: 2C2A  Structure of DesK HK module H188V mutant in complex (Albanesi et al., 2009) Protein Data Bank accession code: 3EHH  with ADP  Software and Algorithms  PHENIX (Adams et al., 2010) https://www.phenix-online.org  STARANISO (Tickle et al., 2010) https://www.phenix-online.org  COOT (Emsley et al., 2010) https://www.cgl.ucsf.edu/chimera	REAGENT or RESOURCE	SOURCE	IDENTIFIER
Bacterial and Virus Strains  Staphylococcus aureus strain RN4220 Richard Novick N/A  Staphylococcus aureus strain RN9011 Richard Novick N/A  Biological Samples  Plasmid for membrane scaffold protein MSP1E3D1 Addgene #20066 site-specific integration suicide vector pJC1111 Richard Novick N/A  Chemicals, Peptides, and Recombinant Proteins FAM-AIP-I Tom Muir; (Lyon et al., 2002) N/A  Deposited Data  Structure of GCN4-AgrC <sub>209</sub> fusion chimera (anisotropic cutoff) this paper Protein Data Bank accession code: 6E52 Structure of GCN4-AgrC <sub>209</sub> fusion chimera (isotropic cutoff) this paper Protein Data Bank accession code: 6E95 Structure of AgrC CA domain (Srivastava et al., 2014) Protein Data Bank accession code: 4BXI  Structure of EnvZ HK chimera with the DHp connector loop (Casino et al., 2014) Frotein Data Bank accession code: 4KP4 of HK853 Structure of CpxA HK module with ATP bound (Mechaly et al., 2014) Protein Data Bank accession code: 2C2A Structure of DesK HK module H188V mutant in complex (Albanesi et al., 2005) Rotein Data Bank accession code: 3EHH with ADP Software and Algorithms PHENIX (Adams et al., 2010) https://www.phenix-online.org  STARANISO (Tickle et al., 2010) https://www.phenix-online.org  Https://www.phenix-online.org  Https://www.phenix-online.org  Https://www.phenix-online.org  Https://www.cgl.ucsf.edu/chimera	Antibodies		
Staphylococcus aureus strain RN4220 Richard Novick N/A  Staphylococcus aureus strain RN9011 Richard Novick N/A  Staphylococcus aureus strain RN7206 Richard Novick N/A  Biological Samples  Plasmid for membrane scaffold protein MSP1E3D1 Addgene #20066  site-specific integration suicide vector puC11111 Richard Novick N/A  Chemicals, Peptides, and Recombinant Proteins  FAM-AIP-I Tom Muir; (Lyon et al., 2002) N/A  Deposited Data  Structure of GCN4-AgrC200 fusion chimera (anisotropic cutoff) this paper Protein Data Bank accession code: 6E52  Structure of GCN4-AgrC200 fusion chimera (isotropic cutoff) this paper Protein Data Bank accession code: 6E95  Structure of AgrC CA domain (Srivastava et al., 2014) Protein Data Bank accession code: 4BXI  Structure of EnvZ HK chimera with the DHp connector loop (Casino et al., 2014) Protein Data Bank accession code: 4KP4 of HK853  Structure of CpxA HK module with ATP bound (Mechaly et al., 2014) Protein Data Bank accession code: 4BIV  Structure of Desk HK module H188V mutant in complex (Albanesi et al., 2009) Protein Data Bank accession code: 2C2A  Structure of Desk HK module H188V mutant in complex (Albanesi et al., 2009) Protein Data Bank accession code: 3EHH with ADP  Software and Algorithms  PHENIX (Adams et al., 2010) https://www.phenix-online.org  STARANISO (Tickle et al., 2018) http://staraniso.globalphasing.org  COOT (Emsley et al., 2010) https://www.cgl.ucsf.edu/chimera	Rabbit anti-pHis polyclonal antibody	(Kee et al., 2013)	N/A
Staphylococcus aureus strain RN9011 Richard Novick N/A  Staphylococcus aureus strain RN7206 Richard Novick N/A  Escherichia coli B834 (DE3) Fred Hughson N/A  Biological Samples  Plasmid for membrane scaffold protein MSP1E3D1 Addgene #20066 site-specific integration suicide vector pJC1111 Richard Novick N/A  Chemicals, Peptides, and Recombinant Proteins  FAM-AIP-I Tom Muir; (Lyon et al., 2002) N/A  Deposited Data  Structure of GCN4-AgrC <sub>209</sub> fusion chimera (anisotropic cutoff) this paper Protein Data Bank accession code: 6E52 Structure of AgrC CA domain (Srivastava et al., 2014) Protein Data Bank accession code: 4BXI  Structure of EnvZ HK chimera with the DHp connector loop of HK853  Structure of CPA HK module with ATP bound (Mechaly et al., 2014) Protein Data Bank accession code: 4BIV  Structure of DesK HK module H188V mutant in complex (Albanesi et al., 2009) Protein Data Bank accession code: 3EHH with ADP  Software and Algorithms  PHENIX (Adams et al., 2010) https://www.phenix-online.org  STARANISO (Tickle et al., 2018) https://www.phenix-online.org  STARANISO (Pettersen et al., 2004) https://www2.mrc-lmb.cam.ac.uk/personal/pemsley/coot  UCSF Chimera (Pettersen et al., 2004) https://www2.mrc-lmb.cam.ac.uk/personal/pemsley/coot	Bacterial and Virus Strains		
Staphylococcus aureus strain RN7206 Richard Novick N/A  Escherichia coli B834 (DE3) Fred Hughson N/A  Biological Samples  Plasmid for membrane scaffold protein MSP1E3D1 Addgene #20066  site-specific integration suicide vector pJC1111 Richard Novick N/A  Chemicals, Peptides, and Recombinant Proteins  FAM-AIP-I Tom Muir; (Lyon et al., 2002) N/A  Deposited Data  Structure of GCN4-AgrC <sub>209</sub> fusion chimera (anisotropic cutoff) this paper Protein Data Bank accession code: 6E52  Structure of AgrC CA domain (Srivastava et al., 2014) Protein Data Bank accession code: 4BXI  Structure of EnvZ HK chimera with the DHp connector loop (Casino et al., 2014) Protein Data Bank accession code: 4KP4 of HK853  Structure of CPXA HK module with ATP bound (Mechaly et al., 2014) Protein Data Bank accession code: 4BIV  Structure of Desk HK module H188V mutant in complex (Albanesi et al., 2009) Protein Data Bank accession code: 2C2A  Structure of Desk HK module H188V mutant in complex (Marina et al., 2009) Protein Data Bank accession code: 3EHH with ADP  Software and Algorithms  PHENIX (Adams et al., 2010) https://wwww.phenix-online.org  STARANISO (Tickle et al., 2018) https://wwww.pm.c-lmb.cam.ac.uk/personal/pemsley/coot  UCSF Chimera (Pettersen et al., 2004) https://wwww.gl.ucsf.edu/chimera	Staphylococcus aureus strain RN4220	Richard Novick	N/A
Escherichia coli B834 (DE3)  Fred Hughson  N/A  Biological Samples  Plasmid for membrane scaffold protein MSP1E3D1  Addgene  #20066  site-specific integration suicide vector pJC1111  Richard Novick  N/A  Chemicals, Peptides, and Recombinant Proteins  FAM-AIP-I  Tom Muir; (Lyon et al., 2002)  N/A  Deposited Data  Structure of GCN4-AgrC <sub>209</sub> fusion chimera (anisotropic cutoff)  this paper  Protein Data Bank accession code: 6E52  Structure of AgrC CA domain  Structure of AgrC CA domain  Structure of EnvZ HK chimera with the DHp connector loop  of HK853  Structure of CPXA HK module with ATP bound  (Mechaly et al., 2014)  Protein Data Bank accession code: 4KP4  Structure of PK853 HK module  (Marina et al., 2005)  Protein Data Bank accession code: 2C2A  Structure of DesK HK module H188V mutant in complex  (Albanesi et al., 2009)  Protein Data Bank accession code: 3EHH  with ADP  Software and Algorithms  PHENIX  (Adams et al., 2010)  https://www.phenix-online.org  https://staraniso.globalphasing.org  COOT  (Emsley et al., 2010)  https://www.cgl.ucsf.edu/chimera	Staphylococcus aureus strain RN9011	Richard Novick	N/A
Biological Samples  Plasmid for membrane scaffold protein MSP1E3D1 Addgene #20066  site-specific integration suicide vector pJC1111 Richard Novick N/A  Chemicals, Peptides, and Recombinant Proteins  FAM-AIP-I Tom Muir; (Lyon et al., 2002) N/A  Deposited Data  Structure of GCN4-AgrC <sub>200</sub> fusion chimera (anisotropic cutoff) this paper Protein Data Bank accession code: 6E52  Structure of GCN4-AgrC <sub>200</sub> fusion chimera (isotropic cutoff) this paper Protein Data Bank accession code: 6E95  Structure of AgrC CA domain (Srivastava et al., 2014) Protein Data Bank accession code: 4BXI  Structure of EnvZ HK chimera with the DHp connector loop (Casino et al., 2014) Protein Data Bank accession code: 4KP4  of HK853  Structure of CpxA HK module with ATP bound (Mechaly et al., 2014) Protein Data Bank accession code: 4BIV  Structure of HK853 HK module (Marina et al., 2005) Protein Data Bank accession code: 2C2A  Structure of Desk HK module H188V mutant in complex (Albanesi et al., 2009) Protein Data Bank accession code: 3EHH  with ADP  Software and Algorithms  PHENIX (Adams et al., 2010) https://www.phenix-online.org  STARANISO (Tickle et al., 2018) http://staraniso.globalphasing.org  COOT (Emsley et al., 2010) https://www.gl.ucsf.edu/chimera	Staphylococcus aureus strain RN7206	Richard Novick	N/A
Plasmid for membrane scaffold protein MSP1E3D1 Addgene #20066 site-specific integration suicide vector pJC1111 Richard Novick N/A  Chemicals, Peptides, and Recombinant Proteins  FAM-AIP-I Tom Muir; (Lyon et al., 2002) N/A  Deposited Data  Structure of GCN4-AgrC <sub>209</sub> fusion chimera (anisotropic cutoff) this paper Protein Data Bank accession code: 6E52 Structure of GCN4-AgrC <sub>209</sub> fusion chimera (isotropic cutoff) this paper Protein Data Bank accession code: 6E95 Structure of AgrC CA domain (Srivastava et al., 2014) Protein Data Bank accession code: 4BXI Structure of EnvZ HK chimera with the DHp connector loop (Casino et al., 2014) Protein Data Bank accession code: 4KP4 of HK853 Structure of CpxA HK module with ATP bound (Mechaly et al., 2014) Protein Data Bank accession code: 4BIV Structure of HK853 HK module (Marina et al., 2005) Protein Data Bank accession code: 2C2A Structure of DesK HK module H188V mutant in complex (Albanesi et al., 2009) Protein Data Bank accession code: 3EHH with ADP Software and Algorithms  PHENIX (Adams et al., 2010) https://www.phenix-online.org STARANISO (Tickle et al., 2018) http://www.phenix-online.org COOT (Emsley et al., 2010) https://www.cgl.ucsf.edu/chimera	Escherichia coli B834 (DE3)	Fred Hughson	N/A
Structure of EnvZ HK chimera with the DHp connector loop of HK853  Structure of CpxA HK module with ATP bound (Mechaly et al., 2014)  Structure of Desk HK module H188V mutant in complex with ADP  Software and Algorithms  PHENIX  (Adams et al., 2010)  STARANISO  (Pettersen et al., 2010)  Richard Novick  N/A  N/A  Richard Novick  N/A  Richard Novich  Richa	Biological Samples		
Chemicals, Peptides, and Recombinant Proteins  FAM-AIP-I  Deposited Data  Structure of GCN4-AgrC <sub>209</sub> fusion chimera (anisotropic cutoff) this paper Protein Data Bank accession code: 6E52  Structure of GCN4-AgrC <sub>209</sub> fusion chimera (isotropic cutoff) this paper Protein Data Bank accession code: 6E95  Structure of AgrC CA domain (Srivastava et al., 2014) Protein Data Bank accession code: 4BXI  Structure of EnvZ HK chimera with the DHp connector loop (Casino et al., 2014) Protein Data Bank accession code: 4KP4  of HK853  Structure of CpxA HK module with ATP bound (Mechaly et al., 2014) Protein Data Bank accession code: 4BIV  Structure of HK853 HK module (Marina et al., 2005) Protein Data Bank accession code: 2C2A  Structure of DesK HK module H188V mutant in complex (Albanesi et al., 2009) Protein Data Bank accession code: 3EHH  with ADP  Software and Algorithms  PHENIX (Adams et al., 2010) https://www.phenix-online.org  STARANISO (Tickle et al., 2018) http://staraniso.globalphasing.org  COOT (Emsley et al., 2010) https://www2.mrc-lmb.cam.ac.uk/personal/pemsley/coot  UCSF Chimera (Pettersen et al., 2004) https://www.cgl.ucsf.edu/chimera	Plasmid for membrane scaffold protein MSP1E3D1	Addgene	#20066
FAM-AIP-I  Deposited Data  Structure of GCN4-AgrC <sub>209</sub> fusion chimera (anisotropic cutoff) this paper Protein Data Bank accession code: 6E52  Structure of GCN4-AgrC <sub>209</sub> fusion chimera (isotropic cutoff) this paper Protein Data Bank accession code: 6E95  Structure of AgrC CA domain (Srivastava et al., 2014) Protein Data Bank accession code: 4BXI  Structure of EnvZ HK chimera with the DHp connector loop (Casino et al., 2014) Protein Data Bank accession code: 4KP4  of HK853  Structure of CpxA HK module with ATP bound (Mechaly et al., 2014) Protein Data Bank accession code: 4BIV  Structure of HK853 HK module (Marina et al., 2005) Protein Data Bank accession code: 2C2A  Structure of DesK HK module H188V mutant in complex (Albanesi et al., 2009) Protein Data Bank accession code: 3EHH  with ADP  Software and Algorithms  PHENIX (Adams et al., 2010) https://www.phenix-online.org  STARANISO (Tickle et al., 2018) http://staraniso.globalphasing.org  COOT (Emsley et al., 2010) https://www2.mrc-lmb.cam.ac.uk/personal/pemsley/coot  UCSF Chimera (Pettersen et al., 2004) https://www.cgl.ucsf.edu/chimera	site-specific integration suicide vector pJC1111	Richard Novick	N/A
Deposited Data  Structure of GCN4-AgrC <sub>209</sub> fusion chimera (anisotropic cutoff) this paper Protein Data Bank accession code: 6E52  Structure of GCN4-AgrC <sub>209</sub> fusion chimera (isotropic cutoff) this paper Protein Data Bank accession code: 6E95  Structure of AgrC CA domain (Srivastava et al., 2014) Protein Data Bank accession code: 4BXI  Structure of EnvZ HK chimera with the DHp connector loop of HK853  Structure of CpxA HK module with ATP bound (Mechaly et al., 2014) Protein Data Bank accession code: 4BIV  Structure of HK853 HK module (Marina et al., 2005) Protein Data Bank accession code: 2C2A  Structure of DesK HK module H188V mutant in complex (Albanesi et al., 2009) Protein Data Bank accession code: 3EHH with ADP  Software and Algorithms  PHENIX (Adams et al., 2010) https://www.phenix-online.org  STARANISO (Tickle et al., 2018) http://staraniso.globalphasing.org  COOT (Emsley et al., 2010) https://www2.mrc-lmb.cam.ac.uk/personal/pemsley/coot  UCSF Chimera (Pettersen et al., 2004) https://www.cgl.ucsf.edu/chimera	Chemicals, Peptides, and Recombinant Proteins		
Structure of GCN4-AgrC <sub>209</sub> fusion chimera (anisotropic cutoff) this paper Protein Data Bank accession code: 6E52 Structure of GCN4-AgrC <sub>209</sub> fusion chimera (isotropic cutoff) this paper Protein Data Bank accession code: 6E95 Structure of AgrC CA domain (Srivastava et al., 2014) Protein Data Bank accession code: 4BXI Structure of EnvZ HK chimera with the DHp connector loop of HK853 Structure of CpxA HK module with ATP bound (Mechaly et al., 2014) Protein Data Bank accession code: 4BIV Structure of HK853 HK module (Marina et al., 2005) Protein Data Bank accession code: 2C2A Structure of DesK HK module H188V mutant in complex (Albanesi et al., 2009) Protein Data Bank accession code: 3EHH with ADP Software and Algorithms  PHENIX (Adams et al., 2010) https://www.phenix-online.org STARANISO (Tickle et al., 2018) http://staraniso.globalphasing.org COOT (Emsley et al., 2010) https://www2.mrc-lmb.cam.ac.uk/personal/pemsley/coot UCSF Chimera (Pettersen et al., 2004) https://www.cgl.ucsf.edu/chimera	FAM-AIP-I	Tom Muir; (Lyon et al., 2002)	N/A
Structure of GCN4-AgrC209 fusion chimera (isotropic cutoff)  Structure of AgrC CA domain  (Srivastava et al., 2014)  Structure of EnvZ HK chimera with the DHp connector loop of HK853  Structure of CpxA HK module with ATP bound  (Mechaly et al., 2014)  Structure of Desk HK module H188V mutant in complex with ADP  Software and Algorithms  PHENIX  (Adams et al., 2010)  STARANISO  (Tickle et al., 2018)  (Tickle et al., 2010)  (Emsley et al., 2004)  Protein Data Bank accession code: 4BIV  Protein Data Bank accession code: 2C2A  Protein Data Bank accession code: 2C2A  Protein Data Bank accession code: 3EHH  with ADP  Software and Algorithms  PHENIX  (Adams et al., 2010)  https://www.phenix-online.org  https://www2.mrc-lmb.cam.ac.uk/personal/ pemsley/coot  UCSF Chimera  (Pettersen et al., 2004)  https://www.cgl.ucsf.edu/chimera	Deposited Data		
Structure of AgrC CA domain  (Srivastava et al., 2014)  Protein Data Bank accession code: 4BXI  Structure of EnvZ HK chimera with the DHp connector loop of HK853  Structure of CpxA HK module with ATP bound  (Mechaly et al., 2014)  Protein Data Bank accession code: 4KP4  (Mechaly et al., 2014)  Protein Data Bank accession code: 4BIV  Structure of HK853 HK module  (Marina et al., 2005)  Protein Data Bank accession code: 2C2A  Structure of DesK HK module H188V mutant in complex (Albanesi et al., 2009)  Protein Data Bank accession code: 3EHH with ADP  Software and Algorithms  PHENIX  (Adams et al., 2010)  STARANISO  (Tickle et al., 2018)  https://www.phenix-online.org  https://www2.mrc-lmb.cam.ac.uk/personal/ pemsley/coot  UCSF Chimera  (Pettersen et al., 2004)  https://www.cgl.ucsf.edu/chimera	Structure of GCN4-AgrC <sub>209</sub> fusion chimera (anisotropic cutoff)	this paper	Protein Data Bank accession code: 6E52
Structure of EnvZ HK chimera with the DHp connector loop of HK853  Structure of CpxA HK module with ATP bound (Mechaly et al., 2014) Protein Data Bank accession code: 4KP4  Structure of HK853 HK module (Marina et al., 2005) Protein Data Bank accession code: 2C2A  Structure of DesK HK module H188V mutant in complex (Albanesi et al., 2009) Protein Data Bank accession code: 3EHH with ADP  Software and Algorithms  PHENIX (Adams et al., 2010) https://www.phenix-online.org  STARANISO (Tickle et al., 2018) http://staraniso.globalphasing.org  COOT (Emsley et al., 2010) https://www2.mrc-lmb.cam.ac.uk/personal/pemsley/coot  UCSF Chimera (Pettersen et al., 2004) https://www.cgl.ucsf.edu/chimera	Structure of GCN4-AgrC <sub>209</sub> fusion chimera (isotropic cutoff)	this paper	Protein Data Bank accession code: 6E95
of HK853 Structure of CpxA HK module with ATP bound (Mechaly et al., 2014) Protein Data Bank accession code: 4BIV Structure of HK853 HK module (Marina et al., 2005) Protein Data Bank accession code: 2C2A Structure of DesK HK module H188V mutant in complex (Albanesi et al., 2009) Protein Data Bank accession code: 3EHH with ADP Software and Algorithms PHENIX (Adams et al., 2010) https://www.phenix-online.org STARANISO (Tickle et al., 2018) http://staraniso.globalphasing.org COOT (Emsley et al., 2010) https://www2.mrc-lmb.cam.ac.uk/personal/ pemsley/coot UCSF Chimera (Pettersen et al., 2004) https://www.cgl.ucsf.edu/chimera	Structure of AgrC CA domain	(Srivastava et al., 2014)	Protein Data Bank accession code: 4BXI
Structure of HK853 HK module  Structure of DesK HK module H188V mutant in complex With ADP  Software and Algorithms  PHENIX  (Adams et al., 2010)  STARANISO  (Tickle et al., 2018)  COOT  (Emsley et al., 2010)  https://www.phenix-online.org https://www2.mrc-lmb.cam.ac.uk/personal/pemsley/coot  UCSF Chimera  (Pettersen et al., 2004)  https://www.cgl.ucsf.edu/chimera	Structure of EnvZ HK chimera with the DHp connector loop of HK853	(Casino et al., 2014)	Protein Data Bank accession code: 4KP4
Structure of DesK HK module H188V mutant in complex (Albanesi et al., 2009)  With ADP  Software and Algorithms  PHENIX (Adams et al., 2010) https://www.phenix-online.org  STARANISO (Tickle et al., 2018) http://staraniso.globalphasing.org  COOT (Emsley et al., 2010) https://www2.mrc-lmb.cam.ac.uk/personal/pemsley/coot  UCSF Chimera (Pettersen et al., 2004) https://www.cgl.ucsf.edu/chimera	Structure of CpxA HK module with ATP bound	(Mechaly et al., 2014)	Protein Data Bank accession code: 4BIV
with ADP  Software and Algorithms  PHENIX (Adams et al., 2010) https://www.phenix-online.org  STARANISO (Tickle et al., 2018) http://staraniso.globalphasing.org  COOT (Emsley et al., 2010) https://www2.mrc-lmb.cam.ac.uk/personal/pemsley/coot  UCSF Chimera (Pettersen et al., 2004) https://www.cgl.ucsf.edu/chimera	Structure of HK853 HK module	(Marina et al., 2005)	Protein Data Bank accession code: 2C2A
PHENIX (Adams et al., 2010) https://www.phenix-online.org  STARANISO (Tickle et al., 2018) http://staraniso.globalphasing.org  COOT (Emsley et al., 2010) https://www2.mrc-lmb.cam.ac.uk/personal/pemsley/coot  UCSF Chimera (Pettersen et al., 2004) https://www.cgl.ucsf.edu/chimera	Structure of DesK HK module H188V mutant in complex with ADP	(Albanesi et al., 2009)	Protein Data Bank accession code: 3EHH
STARANISO (Tickle et al., 2018) http://staraniso.globalphasing.org  COOT (Emsley et al., 2010) https://www2.mrc-lmb.cam.ac.uk/personal/ pemsley/coot  UCSF Chimera (Pettersen et al., 2004) https://www.cgl.ucsf.edu/chimera	Software and Algorithms		
COOT (Emsley et al., 2010) https://www2.mrc-lmb.cam.ac.uk/personal/pemsley/coot  UCSF Chimera (Pettersen et al., 2004) https://www.cgl.ucsf.edu/chimera	PHENIX	(Adams et al., 2010)	https://www.phenix-online.org
pemsley/coot  UCSF Chimera (Pettersen et al., 2004) https://www.cgl.ucsf.edu/chimera	STARANISO	(Tickle et al., 2018)	http://staraniso.globalphasing.org
( · · · · · · · · · · · · · · · · · · ·	СООТ	(Emsley et al., 2010)	the state of the s
GraphPad Prism https://www.graphpad.com/	UCSF Chimera	(Pettersen et al., 2004)	https://www.cgl.ucsf.edu/chimera
	GraphPad Prism		https://www.graphpad.com/

#### CONTACT FOR REAGENT AND RESOURCE SHARING

Requests and inquires related to reagents used in this study should be directed to and will be fulfilled by the Lead Contact, Tom Muir (muir@princeton.edu).

#### **EXPERIMENTAL MODEL AND SUBJECT DETAILS**

#### **Bacterial Strains**

S. aureus strains (RN4220, RN9011 and RN7206) and plasmid pJC1111 are kind gifts from Dr. Richard Novick's group (New York University). Plasmid pMK014 is from lab stock generated in previous work (Kim et al., 2016), which harbors a mKate2 gene under the constitutive sarA P1 promoter for cell visualization and quantification. The plasmid was electroporated into RN4220 and selected with erythromycin. Subsequently using standard phage transduction techniques, the vector was introduced into RN7206, a group-lagr-null S. aureus strain, to produce a strain with stable red fluorescent protein expression. To integrate agr-I genes containing wild type agrC or agrC-I-R238A onto the chromosome of RN7206, we employed the site-specific integration suicide vector pJC1111. The agr genes under the control of agr P2 promoter were amplified from the genome of group-I S. aureus and cloned in between the SaPI-1 attS sequence of pJC1111, which integrates into the chromosomal attachment site (attC) of S. aureus pathogenicity island 1 (SaPI-1). The R238A mutation in agrC gene was introduced by standard site-directed mutagenesis. pJC1111 plasmid containing agr

genes was introduced by electroporation into RN9011, which expresses the SaPI-1 integrase, and the chromosomal integrants were selected with cadmium. They were then lysed with phage 80α and transduced into RN7206. S. aureus cells were typically cultured in Trypticase soy broth (TSB) supplemented with appropriate antibiotics at 37°C, except for the phage lysis step where the cells were lysed at 30°C.

E. coli strains BL21 (DE3), C43 (DE3) and B834 (DE3) (a kind gift of Dr. Fred Hughson, Princeton University) were used for recombinant protein expression.

#### **METHOD DETAILS**

#### **Protein Production and Nanodisc Assembly**

Cloning of the GCN4-AgrC chimeras and the full-length AgrC-I construct in the pET-based vector has been described previously (Wang et al., 2014a). Mutations were introduced using the QuikChange Site-Directed Mutagenesis kit from Agilent (La Jolla, CA) following standard protocols. All mutants were sequenced by Genewiz, Inc. (South Plainfield, NJ) and confirmed.

Expression and purification of the soluble GCN4-HK fusion chimeras and mutants was carried out essentially as previously reported with minor changes (Wang et al., 2014a). Briefly, the desired GCN4-HK expression vector was transformed into E. coli BL21 (DE3) cells. The bacteria were grown at 37°C in LB medium supplemented with 100 μg/ml ampicillin to OD<sub>600</sub> of 0.8 and then induced with 0.5 mM IPTG at 18°C overnight. Harvested cell pellet was re-suspended in lysis buffer (20 mM HEPES pH 7.5, 100 mM NaCl, 1 mM PMSF) and lysed using a French-press homogenizer. The lysate was cleared by centrifugation at 35,000g for 30 min at 4°C. For His-tagged constructs, the supernatant was applied to a 4 mL Ni-NTA column for standard IMAC purification. Thrombin treatment was applied if removal of the N-terminal hexahistidine tag from GCN4-AgrC chimera was desired. The untagged protein was then further purified by anion exchange chromatography (HiPrep Q column) using a 0-0.6 M NaCl gradient in a buffer containing 20 mM HEPES pH 7.5. Size exclusion chromatography (Superdex75 column) was then used to exchange the protein in buffer containing 20 mM HEPES pH 7.5, 100 mM NaCl, 1 mM TCEP. For Strep-tagged constructs, the supernatant was incubated with 4 mL Strep-Tactin resin at 4°C for 1 h and then transferred into a plastic column. The column was washed with 10 column volumes (CVs) of HEPES buffer (20 mM HEPES pH 7.5, 100 mM NaCl) and eluted with 4 CVs of elution buffer (20 mM HEPES pH 7.5, 100 mM NaCl and 2.5 mM desthiobiotin). Heterodimers of the GCN4-AgrC<sub>207</sub> mutants were prepared by denaturation of the corresponding homodimers at 1 mg/ml with 6 M guanidine hydrochloride. The desired pairing were then mixed in a 1:1 molar ratio and refolded by stepwise dialysis into a final buffer containing 20 mM HEPES pH 7.5, 100 mM NaCl and 1 mM TCEP. The heterodimer was then purified by a tandem purification procedure employing the His-tag and the Strep-tag according to the protocols described above. To produce the selenomethionine substituted GCN4-AgrC<sub>209</sub>, the GCN4-AgrC<sub>209</sub> expression vector was transformed into E. coli B834 (DE3) cells and the SelenoMethionine Medium Complete kit (Molecular Dimensions, Inc.) was used for medium preparation, following the protocol provided therein. Briefly, starter culture in LB was first inoculated in minimal medium containing L-methionine and grown at 37°C overnight. The cells were then pelleted, washed 3 times with sterile PBS, resuspended and inoculated into minimal medium containing L-selenomethionine. Upon OD600 reaching 0.8, the cells were induced with 0.5 mM IPTG at 18°C overnight. Purification of selenomethionine substituted GCN4-AgrC<sub>209</sub> was performed in the same way as the native protein. The molecular weight of all soluble proteins and complete incorporation of selenium were confirmed by ESI-MS.

Expression and purification of full-length AgrC-I has also been described (Wang et al., 2014a). Briefly, full-length AgrC-I (and mutants thereof) was expressed in E. coli C43 (DE3) cells and was extracted from the membrane fraction of the cell lysate using Foscholine-12. The membrane extract was subjected to Ni-NTA purification, followed by Superdex200 size exclusion chromatography. Fractions containing the protein of interest were pooled together for nanodisc assembly. Reconstitution of AgrC-I into lipid nanodisc was performed following the established protocol (Wang et al., 2014a). DMPC and DMPG lipid stocks were prepared at 50 mM concentration in HBST buffer (20 mM HEPES pH 7.5, 100 mM NaCl and 1 mM TCEP) containing 150 mM sodium cholate, and pre-mixed in a ratio of DMPC:DMPG = 1:3. Membrane scaffold protein (MSP) MSP1E3D1 was expressed and purified as reported elsewhere (Ritchie et al., 2009). In the pre-assembly mix, MSP was incubated with DMPC/DMPG lipids and the purified AgrC-I was incubated with 0.2% (w/v) Fos-choline-12 separately at room temperature (RT) for 15 min. The two mixtures were then combined at a molar ratio of MSP:dimeric AgrC-I:lipids = 4:1:540 and incubated at 30°C for 30 min. Absorbent Bio-Beads (BioRad) were then added to remove detergent from the system to facilitate spontaneous nanodisc formation. The assembled nanodiscs were further purified on a Ni-NTA column, followed by a Superose 6 size exclusion chromatography step using HBST buffer (20 mM HEPES pH 7.5, 100 mM NaCl, 1 mM TCEP). The peak fractions containing the monodispersed AgrC-I nanodisc were pooled as the final product.

#### **Crystallization and Structure Determination**

X-ray diffraction data were collected for both the native and the selenomethionine substituted GCN4-AgrC<sub>209</sub>. Native GCN4-AgrC<sub>209</sub> crystals were grown at RT using the hanging drop vapor diffusion method by mixing protein solution (10 mg/mL) containing 20 mM HEPES pH 7.5, 100 mM NaCl, 1 mM TCEP with well buffer containing 0.1 M Tris pH 8.0 and 2.8 M NaCl in a 1:1 volume ratio. Selenomethionine substituted GCN4-AgrC<sub>209</sub> crystals were grown similarly, except that micro-seeding technique was used, where 10 mg/mL protein solution was first mixed with well buffer containing 0.1 M Tris pH 8.0 and 1.6 M NaCl in a 1:1 volume ratio, preequilibrated at RT for 6 h and then crystal seed stock was introduced exogenously. These crystals were cryo-protected using a single transfer into mother liquor supplemented with 30% (v/v) glycerol and flash cooled in liquid nitrogen.

SAD data were collected at beam line F1 of the Cornell High Energy Synchrotron Source (CHESS). The structure was determined by a combination of molecular replacement and selenomethionine SAD phases using the program PHASER (McCoy et al., 2007). A model was created from residues 278-430 of the ATP binding domain of *S. aureus* AgrC obtained from the PDB file 4BXI (Srivastava et al., 2014) but was insufficient to solve the structure. This initial model was modified iteratively by running molecular replacement trials using models where contiguous sections of the structure were deleted. The log likelihood gain of the putative molecular replacement solution was used as the score for each round. The best scoring model was then subjected to more segment deletions in the next round. After five rounds of deletions the optimized molecular replacement model provided a consistent solution but only found one of the two molecules expected in the asymmetric unit. The partial molecular replacement solution was improved using the MR-SAD method implemented in PHASER in combination with a selenomethionine SAD dataset to 3.1 Å resolution (Table S1). Fifteen Se site locations were found based on initial model phases, with a final figure of merit of 0.48.

The model was rebuilt into the MR-SAD map using COOT (Emsley et al., 2010), followed by refinement using phenix.refine (Adams et al., 2010) and recalculation of the MR-SAD map with the improved model. Native data extending to 2.25 Å were introduced into the refinement and the second molecule in the asymmetric unit became apparent with non-crystallographic symmetry restraints included in refinement. Model improvement stalled until the resolution limits of the highly anisotropic native data set were reconsidered using the STARANISO server at <a href="http://staraniso.globalphasing.org">http://staraniso.globalphasing.org</a> (Tickle et al., 2018). While the original isotropic resolution cutoff applied to this data was 2.25 Å, the maximum resolution of the anisotropic cutoff was 1.93 Å, which provided a small but significant improvement of map interpretability. The native data subsequently used for refinement had an anisotropic cutoff of 2.87 Å along a\*, 2.19 Å along b\* and 1.93 Å along c\*. There are 37,528 native data to 2.25 Å using the isotropic cutoff (resulting in a model deposited as PDB: 6E95) and 36,929 native data to 1.93 Å using the anisotropic cutoff (resulting in a model deposited as PDB: 6E52). Model building was done using COOT and was refined against the native data using REFMAC5 (Murshudov et al., 2011). Molecular graphics were prepared with UCSF Chimera (Pettersen et al., 2004).

#### **Autokinase Assays**

Autokinase reactions were performed as previously described with minor modifications (Wang et al., 2014a). All reactions were carried out in reaction buffer containing 50 mM Tris-HCl, 15 mM HEPES-Na pH 7.8, 100 mM NaCl, 10 mM MgCl<sub>2</sub> and 1 mM TCEP. For analysis using autoradiography and scintillation counting, 2  $\mu$ M GCN4-AgrC chimera or 0.7  $\mu$ M AgrC-I nanodisc was incubated with 10  $\mu$ M [ $\gamma$ -<sup>32</sup>P]-ATP (10Ci/mmol) in reaction buffer at 37°C for 40 min. AlPs were included as indicated to a final concentration of 10  $\mu$ M. For autoradiography, the reaction mixture was mixed with SDS-PAGE loading dye and resolved on 12% Tris-HCI SDS-PAGE gel. The gel was dried using a slab gel dryer (Hoefer, Inc.) and subsequently exposed to Carestream Kodak Biomax XAR film (Sigma-Aldrich) for signal detection. For scintillation counting, a 6  $\mu$ L aliquot of the reaction mixture was spotted on a nitrocellulose membrane (Thermo Scientific), air dried and washed 4 times with TBST buffer (20 mM Tris pH 8.0, 150 mM NaCl and 0.1% (v/v) Tween-20). The dried membrane was transferred to a counting vial containing 3.5 mL Ultima Gold<sup>TM</sup> scintillation cocktail (Perkin Elmer) and the activity was quantified using a MicroBeta2 scintillation counter (Perkin Elmer). For analysis by immuno-blotting, 5  $\mu$ M GCN4-AgrC<sub>207</sub> was incubated with 10 mM cold ATP in reaction buffer at 37°C for 3 min. The reaction was mixed with native gel loading buffer on ice and immediately resolved on a 10% Tris-HCl native-PAGE gel. The amount of histidine phosphorylation was detected using a pan-specific anti-pHis polyclonal antibody (Kee et al., 2013).

#### **Cysteine Accessibility Assay**

Maleimide PEG5K (Nanocs) was prepared as a 1 mM stock in buffer containing 20 mM HEPES pH 7.5, 100 mM NaCl. 1  $\mu$ M cysteine mutant of the GCN4-HK fusion chimeras were incubated with 0.2 mM maleimide PEG5K in 25  $\mu$ L assay buffer containing 20 mM HEPES pH 7.5, 100 mM NaCl and 16  $\mu$ M TCEP at 37°C for 3 min. The reaction was subsequently quenched on ice by addition of 1  $\mu$ L 100 mM DTT and resolved on a 12% Tris-HCl SDS-PAGE gel. The gel was stained with Coomassie Brilliant Blue and the band intensity corresponding to the labeled and the unlabeled species was quantified using an Odyssey Imager (LI-COR Biosciences).

#### **Cysteine Crosslinking of AgrC-I Nanodisc**

The inter-protomer cysteine crosslinking protocol has been detailed previously (Wang et al., 2014a). Briefly, 1  $\mu$ M AgrC-I nanodiscs in buffer containing 20 mM HEPES pH 7.0, 100 mM NaCl and 0.2 mM TCEP were pre-incubated with either 10  $\mu$ M AlP ligand or DMSO as specified. Then glutathione disulfide (GSSG) was added to a final concentration of 10 mM and the reaction mixture was incubated at 37°C for 20 min. Reactions were quenched by addition of thiol-free SDS-PAGE loading dye and the mixtures were resolved on a 15% Tris-HCI SDS-PAGE gel. The band intensity of the AgrC-I crosslinked dimer was quantified using an Odyssey Imager (LI-COR Biosciences) and normalized against that of MSP. In the non-oxidized controls, nanodiscs were first mixed with thiol-free SDS-PAGE loading dye and then glutathione disulfide was added.

#### Fluorescence Anisotropy-Based Binding Assay

FAM-AIP-I was synthesized as described previously (Lyon et al., 2002). Measurement of equilibrium binding between AgrC-I Q305A nanodiscs and FAM-AIP-I and competitive binding of AIP-I and AIP-II followed the protocol outlined previously (Wang et al., 2014a). In deriving the  $K_d$  of AgrC-I Q305A nanodisc binding to FAM-AIP-I, the corrected anisotropy change ( $\Delta$ SSA $^c$ ) was used to control for

light scattering effects caused by AgrC nanodiscs. ASSAc was plotted against AgrC-I Q305A nanodisc concentration ([nanodisc]) and the dataset was fit to one-site specific binding model, treating AgrC-I Q305A nanodisc as the ligand:

$$\Delta SSA^c \ = \ \Delta r_{max} * \frac{[nanodisc]}{[nanodisc] + K_d},$$

where  $\Delta r_{max}$  is the maximal change in fluorescence anisotropy when all FAM-AIP-I is bound.

To derive the  $K_{d-AIP}$  of AIP-I and AIP-II binding to AgrC-I Q305A nanodisc, the anisotropy change ( $\Delta$ SSA) was plotted against the concentration of AIP ligand titrated in ([AIP]). The dataset was fit to the implicit equation below describing a competitive ligand binding model:

$$\Delta SSA \, = \, \frac{\Delta r_{max} * \frac{[nanodisc]_t}{[L]_t} * \left( \left[ L \right]_t - \Delta SSA * \frac{[L]_t}{\Delta r_{max}} \right)}{K_d * \left( 1 + \frac{\left[ AIP \right]^h}{K_{d-AIP}^h} \right) + \left( \left[ L \right]_t - \Delta SSA * \frac{[L]_t}{\Delta r_{max}} \right)}, \label{eq:deltaSSA}$$

where  $\Delta r_{max}$  is the maximal change in fluorescence anisotropy when all FAM-AIP-I is bound, [nanodisc]<sub>t</sub> is the total nanodisc concentration, [L]t is the total concentration of FAM-AIP-I, Kd is the dissociation constant of FAM-AIP-I from AgrC-I Q305A nanodisc and h is the apparent Hill coefficient of AIP ligand binding to AgrC-I Q305A nanodisc. All curve fittings were performed using GraphPad Prism (GraphPad Software).

#### **Biofilm Analysis by Microscope Imaging**

Different S. aureus strains harboring constitutively expressed mKate2 on a chromosome were initially seeded in microfluidic chambers (cross-sectional dimensions of 400 µm x 100 µm x 2 cm (W x H x L)), which were fabricated and prepared as previously described (Kim et al., 2016). The cells were allowed to settle onto the surfaces for 10 min, after which sterile tryptic soy broth (TSB, Difco) containing 3% NaCl was flowed steadily into the devices for 8 h. At t = 8 h, the remaining biofilms were imaged with confocal microscopy. Imaging was performed using a Nikon Eclipse Ti inverted microscope (Melville, NY) fitted with a Yokogawa CSU X-1 confocal spinning disk scanning unit (Biovision Technologies, Exton, PA) and DU-897 X-9351 camera (Andor, Concord, MA). A laser line at 592 nm was used to excite the mKate2 fluorescent protein. Both a 100× oil objective with N.A. 1.4 (Nikon, Melville, NY) and a 1.5x lens placed between the CSU X-1 and the Nikon microscope side port were used. Biofilms were analyzed for cell counts with custom code written in Matlab (Mathworks, Natick, MA) as previously described (Kim et al., 2017). Briefly, each biofilm image was segmented in the z-plane and assessed independently. To calculate cell counts, the constitutive mKate2 fluorescence from the total imaged bacterial biomass area was summed and divided by the experimentally determined average fluorescence signal of single cells. In order to get the average fluorescence signal of single cells, individual cells were recognized and segmented using a watershed-based algorithm. In each area of an individual cell the constitutive mKate2 fluorescence was measured, subtracted from background noise and total signals were summed. A few thousand of individual cells were analyzed to get the average fluorescence signal. Cells in biofilms covering a surface area of 100 × 100 μm<sup>2</sup> were imaged at four different regions for each chamber in n = 4 independent experiments. Each replicate was performed using independent bacterial cultures and independent chambers at RT.

#### **QUANTIFICATION AND STATISTICAL ANALYSIS**

Details on the statistical analysis performed are mentioned in the figure legends.

#### **DATA AND SOFTWARE AVAILABILITY**

#### **Data Resources**

The structural factors and the coordinates of GCN4-AgrC<sub>209</sub> have been deposited in the Protein Data Bank with accession codes, 6E52 (anisotropically truncated dataset) and 6E95 (isotropically truncated dataset).